

Maximum Likelihood Estimation for Alamouti Encoded OQPSK Transmission over Aeronautical Telemetry Data Link

A Dissertation

*Submitted in partial fulfillment of
the requirements for the award of the degree*

of

Master of Technology

in

ELECTRONICS AND COMMUNICATION ENGINEERING

(With Specialization in Communication Systems)

By

Ravindra Mohan Nigam

(Enrollment No. 17531014)



DEPARTMENT OF ELECTRONICS AND COMMUNICATION ENGINEERING

INDIAN INSTITUTE OF TECHNOLOGY,ROORKEE

ROORKEE-247667(INDIA)

JUNE 2019

CANDIDATE'S DECLARATION

I hereby declare that the work presented in this dissertation with title “**Maximum Likelihood Estimation for Alamouti Encoded OQPSK Transmission over Aeronautical Telemetry Data Link**” towards the fulfillment of the requirement for the award of the degree of **Master of Technology** with specialization in **Communication Systems**, submitted in the **Department of Electronics and Communication Engineering, Indian Institute of Technology Roorkee, India** is an authentic record of my own work carried out under the guidance and supervision of **Dr. P. M. Pradhan**, Assistant Professor, Department of Electronics and Communication Engineering, Indian Institute of Technology Roorkee, India.

The content of this dissertation has not been submitted by me for the award of any other degree of this or any other Institute.

Date :

Place :

(**Ravindra Mohan Nigam**)

Enrollment No. 17531014

ECE Department

IIT Roorkee

CERTIFICATE

This is to certify that the statement made by the candidate is correct to the best of my knowledge and belief.

Date :

Place :

(**Dr. P. M. Pradhan**)

Assistant Professor

ECE Department

IIT Roorkee

ACKNOWLEDGEMENT

On completion of my dissertation, I would like to express my deepest gratitude to my supervisor, **Dr. P.M. Pradhan** (Assistant Professor, Department of Electronics and Communication Engineering) for his constant guidance, motivation and support. Throughout my thesis working period, he provided encouragement, sound advice, good teaching and lots of good ideas. He always managed to spare time for his student's research queries despite his extremely busy schedule.

I would like to take this opportunity to express my profound gratitude to my guide not only for his academic guidance but also for his interest in my project. Finally, I am very grateful to my Institution and colleagues whose constant encouragement served to renew my spirit. I wish to avail myself of this opportunity to express a sense of gratitude and love to my friends and my beloved parents for their support and strength.

Date :

Place :

(Ravindra Mohan Nigam)

Abstract

For aircraft flight testing, telemetry data plays a major role in evaluating the performance of the aircraft in real time while ensuring flight safety. Maintaining the data continuity during the entire course of the flight is mandatory considering the risk involved in flight testing. To achieve this, two antennas are generally installed (one at back and another one at belly of the aircraft), which provide approximately omni-directional data coverage for telemetry data transmission. However, the structure of the aircraft may obstruct transmission from any one of the antennas to the ground telemetry station. Problem arises when the signal received from both the on-board antennas are of same magnitude and opposite phase. In this situation, the signal may cancel each other at the receiver leading to self-interference. This phenomenon is termed as “two-antenna problem” in aeronautical telemetry.

To combat the self-interference, transmission from both the antennas can be realized on two different frequencies. Since this method increases transmission bandwidth by two times, it is rarely used. As an alternative, continuous antenna beam steering (considering both antennas as antenna array) can be performed to direct the signal towards telemetry station. This method is mechanically complex, and requires continuous update on the precise telemetry location with reference to aircraft. Alternate solutions have been investigated to solve aforementioned self-interference issue. Space time code (STC) is one such solution which promises to deal with the “two-antenna problem”. One of the variant of STC, specific to the case of two transmit and one receive antennas, is called Alamouti code. In this code, two consecutive symbols are simultaneously transmitted from both the antennas in the first time slot. In the next time slot, same two symbols are transmitted in such a way that they are orthogonal to the symbols transmitted in the previous time slot.

Shaped Offset Quadrature Phase Shift Keying (SOQPSK-TG) and Feher’s Quadrature Phase Shift Keying (FQPSK-B and FQPSK-JR) are standard modulation schemes

used in aeronautical telemetry. As these schemes are nonlinear in nature, application of Alamouti codes is not obvious. Alamouti encoded symbols are used to modulate the CPM phase states of the modulation scheme.

As the STC encoded signals from the two antennas pass through the channel, they get exposed to channel impairments (frequency offset, channel attenuation and time delay). Detection of the signal at the receiver needs estimation of these three parameters. In this thesis, estimation of these three parameters is carried out by placing pilot bits in the transmitted signals. A joint maximum likelihood (ML) estimation of these unknown parameters is carried out and analyzed. Since the joint ML estimator needs a complex 3-Dimensional search, a sequential estimator requiring a less complex search is derived and analyzed. The performances of both joint as well as sequential ML estimators are found to be satisfactory and meeting the Cramér–Rao bound (CRB) criteria.

Due to partial response nature of SOQPSK-TG frequency pulse (spanning across 8 bit period), maximum likelihood sequence estimation (MLSE) has 512 states. Implementation of branch metric calculation for 512 states is highly complex. Pulse shaping has been carried out to generate the SOQPSK-TG approximation, which is subsequently used in the sequential estimator. CPM approximation of FQPSK-JR has also been considered as another candidate for pulse shaping. The mean squared error (MSE) performances for both of these schemes are found to be satisfactory and meeting the CRB criteria. As both of these schemes use frequency pulse spanning across 2 bit periods, STC decoder based on MLSE has 8 states. Due to the lesser number of states, decoder complexity gets significantly reduced.

Contents

Acknowledgement	ii
Abstract	iii
List of Figures	viii
List of Tables	ix
Abbreviations	x
Symbols and Notations	xi
1 Introduction	1
1.1 Transmission Schemes	1
1.1.1 Single Antenna	2
1.1.2 Dual Antenna	3
1.2 Alamouti Space-Time Code	4
1.3 Tier II Waveforms	7
1.3.1 SOQPSK-TG	8
1.3.2 FQPSK-JR	10
1.3.3 ARTM-CPM	13
2 Literature Survey	16
3 System Model for Estimation	19
3.1 Alamouti-Encoding for SOQPSK-TG	19
3.2 Signal Modeling	22
3.3 Frame Synchronization	23

4	Parameter Estimation for SOQPSK-TG	25
4.1	ML Estimation of Frequency Offset, Timing Delays and Channel Gains .	25
4.2	Joint Estimator	27
4.3	Sequential Estimator	27
4.4	Performance Metric	28
4.5	Simulation Results	29
4.5.1	Joint Estimator	31
4.5.2	Sequential Estimator	31
5	Proposed work	35
5.1	Pulse shaping	35
5.2	Modulation Simulation	39
5.3	Parameter Estimation for STC encoded SOQPSK-2T and FQPSK-JR .	43
5.3.1	Simulation Results	43
6	Conclusions and Future Work	49
	Appendix A Cramér–Rao Bound	50

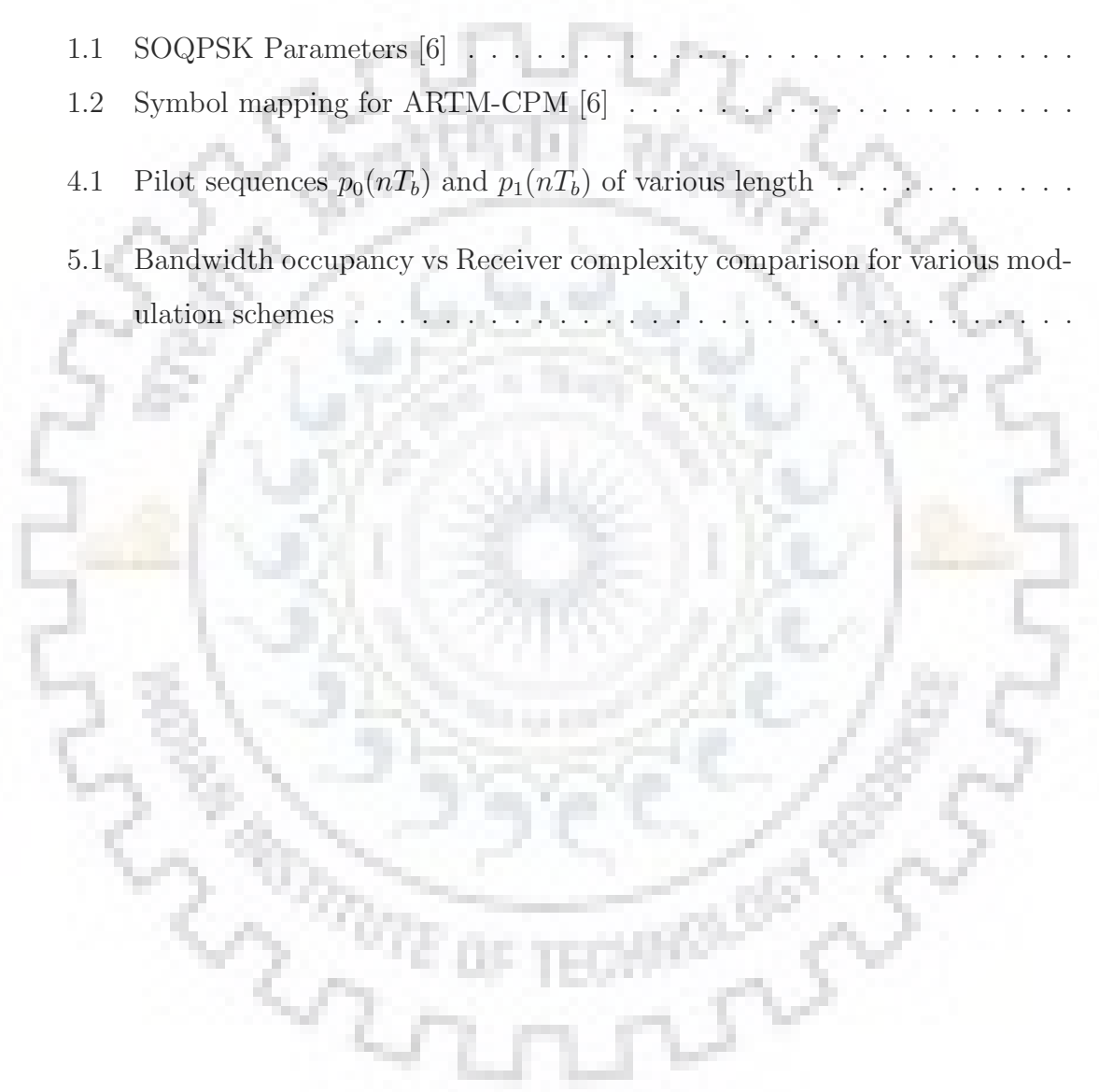
List of Figures

1.1	Interference patterns caused by antenna separations distance of 0.5λ , λ , 5λ , and 10λ wavelengths [1]	2
1.2	Abstract model for Alamouti space-time coding	4
1.3	Alamouti encoding	5
1.4	Block schematic for pre-coded CPM modulator	8
1.5	MATLAB simulation of OQPSK by using CPM method at sampling rate of 2 samples/bit	9
1.6	MATLAB simulation of SOQPSK-TG, SOQPSK-A and SOQPSK-B at 5 kbps data rate: (a) Frequency pulse and phase pulse, (b) Power Spectrum	11
1.7	Simulated frequency pulse $g(t)$ and phase pulse $q(t)$ for FQPSK-JR	13
1.8	Conceptual ARTM-CPM modulator	14
1.9	Simulated frequency pulse $g(t)$ and phase pulse $q(t)$ for ARTM-CPM	15
2.1	Illustration of self interference due to transmission from two antennas [2]	17
3.1	Relation between phase states and trellis states [3]	20
3.2	Relation between SOQPSK-TG four-state approximation, Alamouti STC and bit-level equivalent encoder [4]	20
3.3	Alamouti encoding for SOQPSK-TG [5]	21
3.4	Frame structure	21
3.5	Transmission from aircraft to telemetry station [5]	22
3.6	Non-coherent frame synchronizer for detecting start of pilot sequence [5]	23
4.1	Effect of varying pilot length on CRB. The length of pilot sequence is mentioned as $N_p = N \times L_p$ for $N = 4$	30
4.2	Simulated MSE performance by using joint estimation method for pilot length $L_p = 16$ bits	32


4.3	Simulated MSE performance by using sequential estimation method for pilot length $L_p = 64$ bits	33
5.1	Simulated frequency pulse $g(t)$ and phase pulse $q(t)$ for various modulations	38
5.2	Simulated complex valued samples for various modulations: (a) SOQPSK-TG; (b) FQPSK-JR; (c) SOQPSK-MIL; (d) SOQPSK-6T (Proposed); (e) SOQPSK-4T (Proposed); (f) SOQPSK-2T (Proposed)	40
5.3	Simulated phase trajectory for various modulations: (a) SOQPSK-TG; (b) FQPSK-JR; (c) SOQPSK-MIL; (d) SOQPSK-6T (Proposed); (e) SOQPSK-4T (Proposed); (f) SOQPSK-2T (Proposed)	41
5.4	Simulated power spectrum for various modulations at a data rate of 5 kbps	42
5.5	Simulated MSE performance for FQPSK-JR by using sequential estimation method for display flight	44
5.6	Simulated MSE performance for SOQPSK-2T by using sequential estimation method for display flight	45
5.7	Comparison of MSE performance for SOQPSK-TG, FQPSK-JR and SOQPSK-2T by using sequential estimation method for display flight	46
5.8	Comparison of MSE performance for SOQPSK-TG, FQPSK-JR and SOQPSK-2T by using sequential estimation method for level flight	48

List of Tables

1.1	SOQPSK Parameters [6]	10
1.2	Symbol mapping for ARTM-CPM [6]	14
4.1	Pilot sequences $p_0(nT_b)$ and $p_1(nT_b)$ of various length	29
5.1	Bandwidth occupancy vs Receiver complexity comparison for various modulation schemes	42

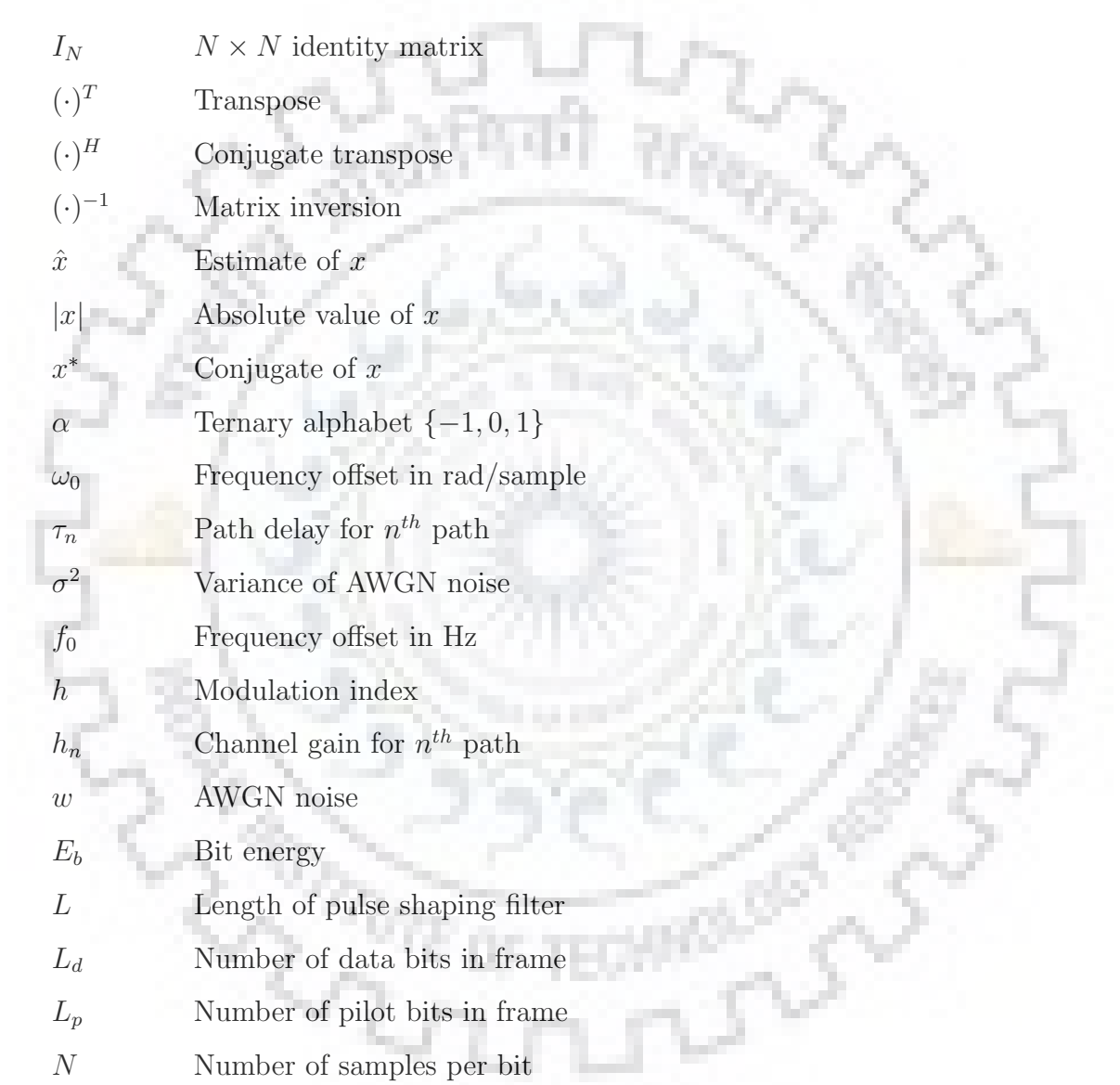


Abbreviations



ARTM	Advanced Range Telemetry
AWGN	Additive White Gaussian Noise
CPFSK	Continuous Phase Frequency Shift Keying
CPM	Continuous Phase Modulation
CRB	Cramér–Rao Bound
FQPSK	Feher’s Quadrature Phase Shift Keying
IID	Independent and Identically Distributed
I-Q	Inphase-Quadrature
IRIG	Inter Range Instrumentation Group
LOS	Line-of-Sight
MIMO	Multiple Input Multiple Output
MISO	Multiple Input Single Output
ML	Maximum Likelihood
MLSE	Maximum Likelihood Sequence Estimation
MSE	Mean Squared Error
OQPSK	Offset Quadrature Phase Shift Keying
PCM/FM	Pulse Code Modulation/Frequency Modulation
PDF	Probability Density Function
PSD	Power Spectral Density
QPSK	Quadrature Phase Shift Keying
RF	Radio Frequency
SISO	Single Input Single Output
SNR	Signal to Noise Ratio
SOQPSK-TG	Shaped Offset Quadrature Phase Shift Keying-Telemetry Group
STC	Space Time Code
XTCQM	Cross-Correlated Trellis Coded Quadrature Modulation

Symbols and Notations



I_N	$N \times N$ identity matrix
$(\cdot)^T$	Transpose
$(\cdot)^H$	Conjugate transpose
$(\cdot)^{-1}$	Matrix inversion
\hat{x}	Estimate of x
$ x $	Absolute value of x
x^*	Conjugate of x
α	Ternary alphabet $\{-1, 0, 1\}$
ω_0	Frequency offset in rad/sample
τ_n	Path delay for n^{th} path
σ^2	Variance of AWGN noise
f_0	Frequency offset in Hz
h	Modulation index
h_n	Channel gain for n^{th} path
w	AWGN noise
E_b	Bit energy
L	Length of pulse shaping filter
L_d	Number of data bits in frame
L_p	Number of pilot bits in frame
N	Number of samples per bit
N_d	Number of data samples in frame
N_p	Number of pilot samples in frame
Q	Quantization parameter for sample time delay
T	Sampling period
T_b	Bit period

Chapter 1

Introduction

The telemetry is a science of collecting data at a place that is remote or inconvenient and to relay this collected data to a place where it can be analyzed [7]. Now-a-days telemetry systems are used in all the areas but traditionally telemetry was mainly used for testing aircraft, missiles, cars and other high velocity systems.

For aircraft flight testing, telemetry data plays a major role to evaluate the performance of the aircraft in real time while ensuring flight safety. Maintaining the data continuity during the entire course of the flight is mandatory considering the risk involved in flight testing.

1.1 Transmission Schemes

Traditionally one antenna was used at the belly of the aircraft, to relay the radio frequency (RF) signal from the aircraft to telemetry station. During flight testing, aircraft will undergo aggressive maneuvering. This behavior may lead to a situations when the channel between on board antenna and telemetry station is obstructed by the aircraft structure itself. This issue is resolved by placing a second antenna on the aircraft so that a clear line-of-sight (LOS) path to the telemetry station from any of the antenna is achieved during all maneuvering conditions. Identical signal is relayed via both the antennas to incorporate redundancy as a solution to single antenna blockage.

As this dual antenna scheme resolves the data outages issue because of single antenna occlusion, the fact that these antennas are placed many wavelengths apart (i.e. installed at different location on the aircraft structure) introduces another problem. It is a known fact from traditional antenna theory that two widely separated antennas will generate a composite radiation pattern having multiple radiation peaks and nulls [1]. This effect

of radiation nulls generation is illustrated in Fig. 1.1 for increasing separation distance (for 0.5λ , λ , 5λ , and 10λ wavelengths) between two antennas. Thus, in the normal flying conditions where none of the antenna is obstructed by the aircraft structure, vehicle maneuvering causes frequent signal loss when radiation pattern null is pointed towards telemetry receiver.

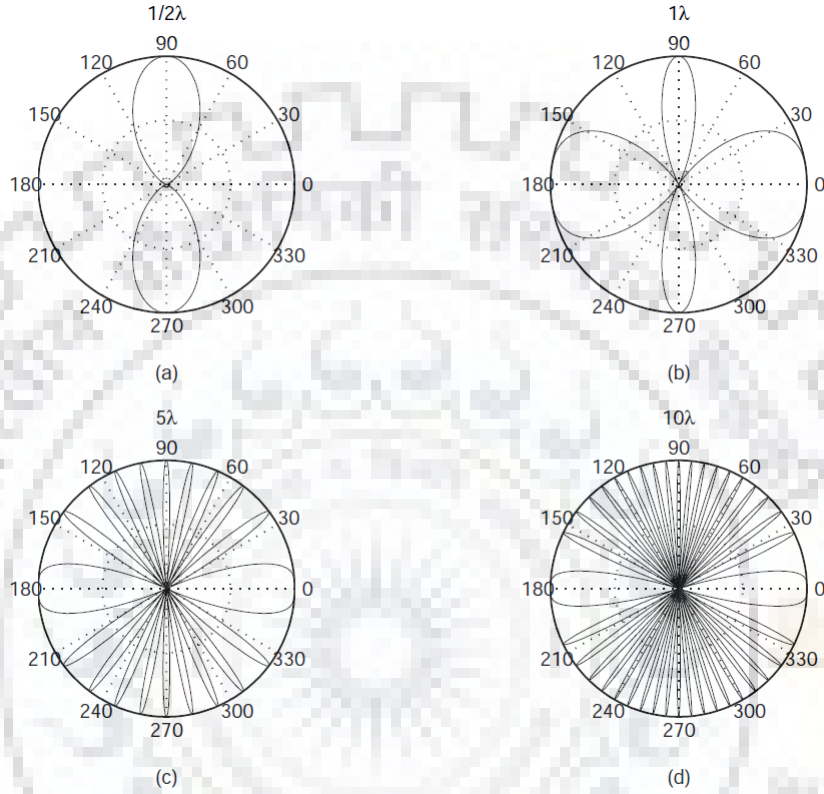


Fig. 1.1. Interference patterns caused by antenna separations distance of 0.5λ , λ , 5λ , and 10λ wavelengths [1]

In the next section, signal to noise ratio (SNR) for the case of single as well as dual antenna transmission is derived and analyzed.

1.1.1 Single Antenna

Single antenna transmission scheme is generally modeled as single input single output (SISO) system. Let us consider symbol x is transmitted from the aircraft to the telemetry station via wireless channel. The received signal in the complex baseband form can be defined as

$$r = hx + \eta \tag{1.1}$$

where h represents complex channel gain and η is complex additive white gaussian noise (AWGN). The energy of the received signal r is

$$E_r = E\{(hx)(hx)^*\} = |h|^2 E_x \quad (1.2)$$

where E_x represents average energy of the transmitted symbols x . Similarly, the noise energy can be expressed as

$$E\{\eta\eta^*\} = \sigma^2 = N_0 \quad (1.3)$$

where σ^2 represents the noise variance of AWGN having noise PSD of N_0 Watt/Hz. The SNR per symbol for single antenna transmission scheme is defined as

$$\text{SNR} = |h|^2 \frac{E_x}{N_0} \quad (1.4)$$

1.1.2 Dual Antenna

Dual antenna transmission scheme is generally modeled as multiple input single output (MISO) system. Traditionally in dual-antenna transmission scheme same signal is fed to both the on board antennas. As both the antennas are placed wide apart, the channel coefficients h_0 and h_1 differ for the two RF signals from each antenna. In this case, the received signal in low pass complex domain is expressed as

$$r = h_0 \frac{x}{\sqrt{2}} + h_1 \frac{x}{\sqrt{2}} + \eta = (h_0 + h_1) \frac{x}{\sqrt{2}} + \eta \quad (1.5)$$

where the $\frac{1}{\sqrt{2}}$ term represents equal power division between both the antennas. The energy of the received signal is defined as

$$\begin{aligned} E_r &= E\{(h_0 + h_1) \frac{x}{\sqrt{2}} (h_0 + h_1)^* \frac{x^*}{\sqrt{2}}\} \\ &= E\{|h_0 + h_1|^2\} E\{|\frac{x}{\sqrt{2}}|^2\} \\ &= \frac{1}{2} |h_0 + h_1|^2 E_x \end{aligned} \quad (1.6)$$

while the noise energy remains same as per (1.3), the effective SNR per symbol for dual antenna case can be defined as

$$\text{SNR} = \frac{E_r}{N_0} = \frac{E_x (|h_0 + h_1|^2)}{2N_0} \quad (1.7)$$

The channel coefficients h_0 and h_1 are generally functions of azimuth and elevation angles describing the receiver direction inside aircraft coordinate frame. The problem associated with this transmission scheme is evident in (1.7). When h_0 and h_1 become equal in magnitude but opposite in phase, the term $|h_0 + h_1|$ reduces to zero. This leads to SNR reduction at the receiver while increasing the error probability.

1.2 Alamouti Space-Time Code

In wireless communication reliability of data transfer is improved by using STC. In this scheme, multiple copies of the same data is transmitted across several antennas. At the receiver, various replicas of the transmitted data are optimally combined to achieve improved SNR. A conceptual model for the two transmitter and one receiver case is shown in Fig. 1.2.

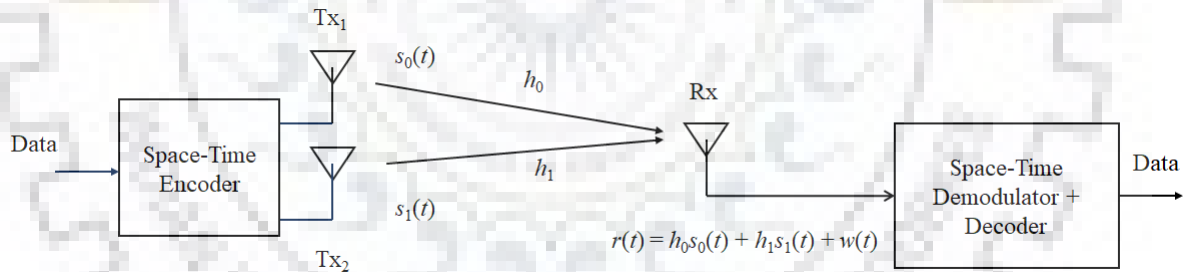


Fig. 1.2. Abstract model for Alamouti space-time coding

The space time coding is a transmit diversity scheme. The signals are transmitted from two different antennas which are different from each other, but both are related to the input data stream. These two signals possess a phase relationship which avoids destructive interference at the receiver. The very first and well-known STC is the Alamouti code, which is a complex orthogonal STC specialized for the case of two transmit antennas. This code was developed by S. Alamouti [8] and was named after him.

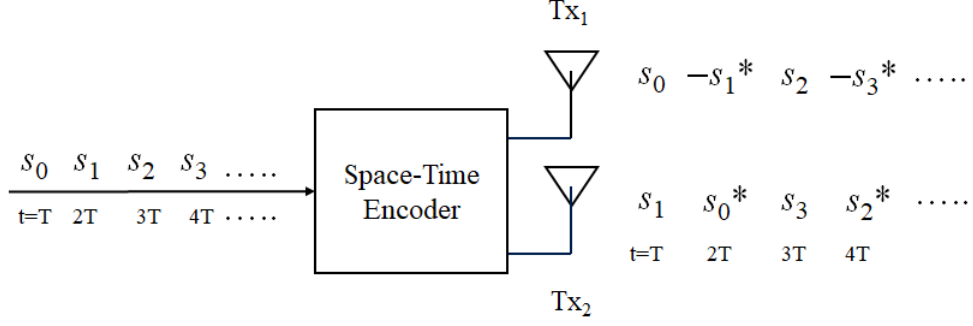


Fig. 1.3. Alamouti encoding

As shown in Fig. 1.3, Alamouti encoded signals are transmitted via two antennas during two symbol intervals. During first symbol interval, symbols s_0 and s_1 are transmitted simultaneously from top and bottom antenna respectively. In the next symbol interval $-s_1^*$ is transmitted from the top antenna and s_0^* transmitted from the bottom antenna. By considering channel coefficients h_0 and h_1 remains constant over the Alamouti period (2 symbol period), the matched filter outputs for the two consecutive symbols is defined as

$$r_0 = h_0 \frac{s_0}{\sqrt{2}} + h_1 \frac{s_1}{\sqrt{2}} + \eta_0 \quad (1.8)$$

$$r_1 = -h_0 \frac{s_1^*}{\sqrt{2}} + h_1 \frac{s_0^*}{\sqrt{2}} + \eta_1^* \quad (1.9)$$

where h_0 and h_1 represents channel coefficients for the two paths (Fig. 1.2), η_0 and η_1 represents complex AWGN for the two received signals. The received vector \mathbf{r} in the form of matrix-vector equation [by taking conjugate of (1.9)] is defined as

$$\begin{aligned} \mathbf{r} &= \begin{bmatrix} r_0 \\ r_1^* \end{bmatrix} \\ &= \frac{1}{\sqrt{2}} \begin{bmatrix} h_0 & h_1 \\ h_1^* & -h_0^* \end{bmatrix} \begin{bmatrix} s_0 \\ s_1 \end{bmatrix} + \begin{bmatrix} \eta_0 \\ \eta_1 \end{bmatrix} \\ &= \frac{1}{\sqrt{2}} \mathbf{H} \mathbf{s} + \boldsymbol{\eta} \end{aligned} \quad (1.10)$$

Note that the Alamouti encoded channel matrix \mathbf{H} is a complex-orthogonal matrix, *i.e.*

$$\begin{aligned}\mathbf{H}^H \mathbf{H} &= \begin{bmatrix} h_0^* & h_1 \\ h_1^* & -h_0 \end{bmatrix} \begin{bmatrix} h_0 & h_1 \\ h_1^* & -h_0^* \end{bmatrix} \\ &= (|h_0|^2 + |h_1|^2) \mathbf{I}_2\end{aligned}\quad (1.11)$$

where \mathbf{I}_2 denotes the 2×2 identity matrix. Because of this orthogonal property, the estimation of transmitted vector can be achieved as

$$\hat{\mathbf{s}} = \mathbf{H}^H \mathbf{r} = \frac{1}{\sqrt{2}} (|h_0|^2 + |h_1|^2) \mathbf{s} + \mathbf{H}^H \boldsymbol{\eta} \quad (1.12)$$

By expanding (1.12), estimation of the transmitted symbols \hat{s}_0 and \hat{s}_1 can be defined as

$$\begin{aligned}\hat{s}_0 &= (|h_0|^2 + |h_1|^2) \frac{s_0}{\sqrt{2}} + h_0^* \eta_0 + h_1 \eta_1 \\ \hat{s}_1 &= (|h_0|^2 + |h_1|^2) \frac{s_1}{\sqrt{2}} + h_1^* \eta_0 - h_0 \eta_1\end{aligned}\quad (1.13)$$

The estimated symbols with minimum euclidean distance will be detected as transmitted symbols. For the first symbol estimate \hat{s}_0 , received signal energy per symbol E_{r_0} is defined as

$$E_{r_0} = \frac{1}{2} E\{(|h_0|^2 + |h_1|^2)^2 s_0 s_0^*\} = \frac{1}{2} (|h_0|^2 + |h_1|^2)^2 E_{s_0} \quad (1.14)$$

and the received noise energy N_{0_0} is defined as

$$\begin{aligned}N_{0_0} &= E\{(h_0^* \eta_0 + h_1 \eta_1)(h_0^* \eta_0 + h_1 \eta_1)^*\} \\ &= |h_0|^2 E\{\eta_0 \eta_0^*\} + |h_1|^2 E\{\eta_1 \eta_1^*\} \\ &= N_0 (|h_0|^2 + |h_1|^2)\end{aligned}\quad (1.15)$$

where $E\{\eta_0 \eta_1\} = 0$ and $N_0 = \sigma_{\eta_0}^2 = \sigma_{\eta_1}^2$. Similarly, signal energy and noise energy for the second symbol estimate \hat{s}_1 is expressed as

$$E_{r_1} = \frac{1}{2} E\{(|h_0|^2 + |h_1|^2)^2 s_1 s_1^*\} = \frac{1}{2} (|h_0|^2 + |h_1|^2)^2 E_{s_1} \quad (1.16)$$

and

$$\begin{aligned}
N_{0_1} &= E\{(h_1^*\eta_0 - h_0\eta_1)(h_1^*\eta_0 - h_0\eta_1)^*\} \\
&= |h_1|^2 E\{\eta_0\eta_0^*\} + |h_0|^2 E\{\eta_1\eta_1^*\} \\
&= N_0(|h_0|^2 + |h_1|^2)
\end{aligned} \tag{1.17}$$

Let us assume $E_s = E_{s_0} = E_{s_1}$. The SNR per symbol for Alamouti encoded dual antenna transmission scheme is defined as

$$\mathbf{SNR} = \frac{E_{r_0}}{N_{0_0}} = \frac{E_{r_1}}{N_{0_1}} = \frac{E_s (|h_0|^2 + |h_1|^2)}{N_0 \cdot 2} \tag{1.18}$$

Recall the SNR expression for traditional MISO scheme (1.7), the term $(|h_0 + h_1|^2)$ is replaced with $(|h_0|^2 + |h_1|^2)$ in case of STC. From these expressions it is evident that h_0 and h_1 can not cancel out each other (to represent destructive interference), as their magnitude gets added in SNR expression for Alamouti's scheme. Thus, Alamouti's scheme is appearing to be immune against antenna masking while avoiding self-interference which is associated with traditional MISO scheme.

1.3 Tier II Waveforms

Traditionally, frequency and phase modulations had been accepted as a primary modulation method in aeronautical telemetry. Since around 1970, Pulse Code Modulation/Frequency Modulation (PCM/FM) had been the most popular modulation scheme in telemetry applications. It is also termed as filtered Continuous Phase Frequency Shift Keying (CPFSK). PCM/FM is generated by passing NRZ-L signal through multi-pole linear phase low pass premodulation filter and then frequency modulating by voltage-controlled oscillator (VCO). The bandwidth of premodulation filter is chosen to be equal to 0.7 times the bit rate. The VCO deviates the carrier by 0.35 times the bit rate to generate PCM/FM. This scheme is not so popular at higher data rates because of limited spectral efficiency.

When higher bandwidth efficiency is needed, the standard modulation schemes for digital data transmission are SOQPSK-TG, FQPSK (FQPSK-B and FQPSK-JR) and the Advanced Range Telemetry (ARTM) Continuous Phase Modulation (CPM). All of these schemes possess constant, or closely constant, envelope characteristics. These schemes

are also suitable to work with non-linear power amplifiers because of attaining minimum spectral regrowth while achieving minimal degradation in detection efficiency.

1.3.1 SOQPSK-TG

SOQPSK-TG belongs to the family of constant envelope CPM waveforms. It is a partial response signaling as the length of frequency pulse (described in [3] and [9]) is 8 bit intervals long. This scheme takes constrained-ternary alphabet as input and has modulation index of $1/2$. The ML detector in the AWGN environment is a MLSE having total number of 512 states [10]. Several method were explored by Perrins for the detection of SOQPSK-TG modulated signal which are described in [3, 9, 11, 12].

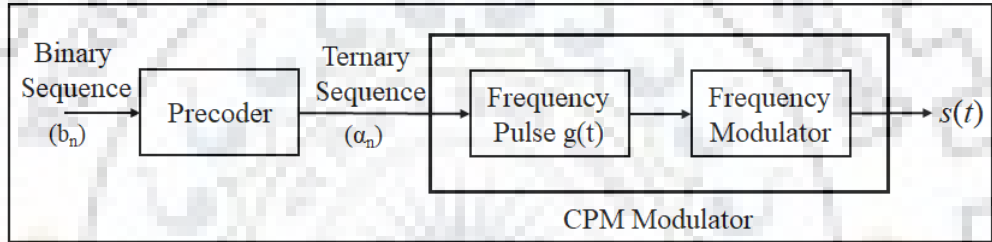


Fig. 1.4. Block schematic for pre-coded CPM modulator

In this section generation of Offset Quadrature Phase Shift Keying (OQPSK) by CPM method is explained followed by generation of SOQPSK. A basic block schematic for the pre-coded CPM modulator is shown in Fig. 1.4. To generate these waveforms pre-coded CPM modulated signal is defined as

$$S(t, \alpha) = \sqrt{\frac{2E_b}{T_b}} \exp[j(\phi(t, \alpha) + \phi_0)] \quad (1.19)$$

where T_b denotes bit interval; E_b denotes energy per bit in the CPM signal and ϕ_0 is an initial phase (can be set to 0). The phase of the signal is expresses as

$$\phi(t, \alpha) = 2\pi h \int_{-\infty}^t \sum_{n=-\infty}^{\infty} \alpha_n g(\tau - nT_b) d\tau = 2\pi h \sum_{n=-\infty}^{\infty} \alpha_n q(t - nT_b) \quad (1.20)$$

where $g(t)$ represents frequency pulse; $q(t) = \int_{-\infty}^t g(\tau) d\tau$ represents phase pulse; $h = 1/2$ is the modulation index; and $\alpha_n \in \{-1, 0, 1\}$ are the ternary symbols which are

related to the binary input symbols $b_n \in \{-1, 1\}$ by [13, 14]

$$\alpha_n = (-1)^{n+1} \frac{b_{n-1}(b_n - b_{n-2})}{2} \quad (1.21)$$

To generate OQPSK, frequency pulse is taken as impulse function i.e., $g(t) = (1/2)\delta(t)$, thus the phase pulse is a step function [$q(t) = (1/2)u(t)$]. MATLAB simulation was carried out to generate the OQPSK using CPM method referred above at a rate of 2 sample/bit. Fig. 1.5(a) and Fig. 1.5(b) illustrates complex valued samples and phase trajectory of OQPSK.

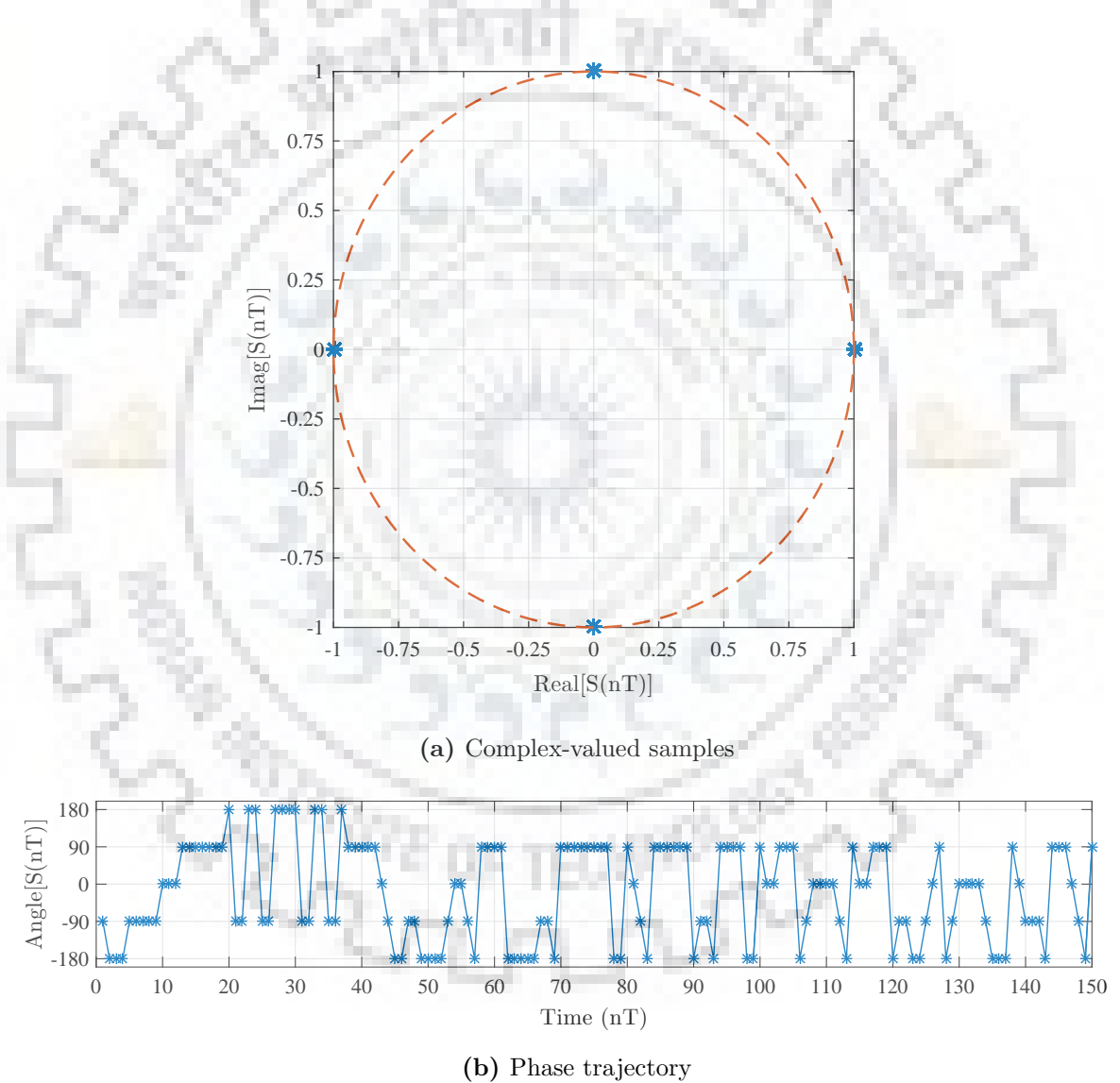


Fig. 1.5. MATLAB simulation of OQPSK by using CPM method at sampling rate of 2 samples/bit

The frequency pulse $g(t)$ used to generate SOQPSK is a modified version of raised cosine function which is being windowed by a temporal raised cosine expressed as

$$g(t) = C \frac{\cos\left(\frac{\pi\rho Bt}{2T_b}\right)}{1 - 4\left(\frac{\rho Bt}{2T_b}\right)^2} \times \frac{\sin\left(\frac{\pi Bt}{2T_b}\right)}{\left(\frac{\pi Bt}{2T_b}\right)} \times w(t) \quad (1.22)$$

for

$$w(t) = \begin{cases} 1 & 0 \leq \left|\frac{t}{2T_b}\right| < T_1 \\ \frac{1}{2} + \frac{1}{2} \cos\left(\frac{\pi}{T_2}\left(\frac{t}{2T_b} - T_1\right)\right) & T_1 \leq \left|\frac{t}{2T_b}\right| \leq T_1 + T_2 \\ 0 & T_1 + T_2 < \left|\frac{t}{2T_b}\right| \end{cases} \quad (1.23)$$

The constant C in $g(t)$ is selected such that $g(t) = 1/2$ for $t \geq 2(T_1+T_2)T_b$. Table 1.1 below shows different values of ρ , B , T_1 , and T_2 to generate different variants of SOQPSK.

Table 1.1: SOQPSK Parameters [6]

SOQPSK Type	ρ	B	T_1	T_2
SOQPSK-A	1	1.35	1.4	0.6
SOQPSK-B	0.5	1.45	2.8	1.2
SOQPSK-TG	0.7	1.25	1.5	0.5

Initially, two variants of SOQPSK namely SOQPSK-A and SOQPSK-B were introduced [15]. SOQPSK-A has narrower spectrum than SOQPSK-B but it suffers from slightly inferior detection efficiency. As a compromise between these two waveform a third version SOQPSK-TG (SOQPSK-Telemetry group) was introduced. This variant was adopted as one of the modulation methods for Inter Range Instrumentation Group (IRIG-106) standard by the Telemetry Group of the Range Commanders Council in 2004. MATLAB simulation of frequency pulse $g(t)$ and phase pulse $q(t)$ of these variants is shown in Fig. 1.6(a). Simulation of comparative power spectrum is shown in Fig. 1.6(b).

1.3.2 FQPSK-JR

FQPSK and its variants belongs to linear modulation methods. This scheme has a close resemblance with the offset modulation as the quadrature (Q) component is delayed by half symbol period from in-phase (I) component. Principally, in this modulation both I and Q waveforms are constrained to be selected from a pool of waveforms. Selection

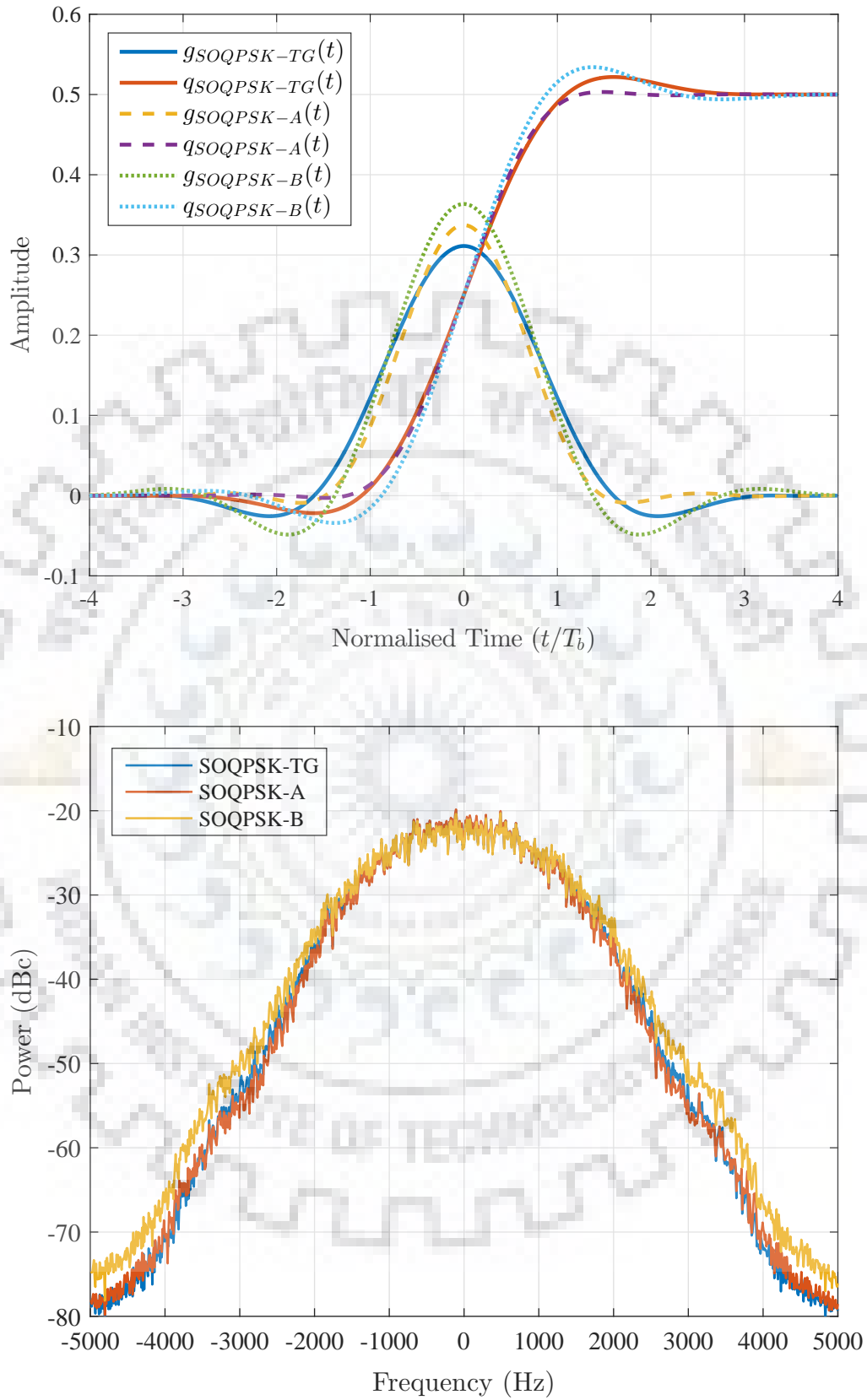


Fig. 1.6. MATLAB simulation of SOQPSK-TG, SOQPSK-A and SOQPSK-B at 5 kbps data rate: (a) Frequency pulse and phase pulse, (b) Power Spectrum

of these waveforms in a constrained way can be devised as a trellis code and formulated in terms of cross-correlated trellis coded quadrature modulation (XTCQM) [16]. Initial variant of this modulation is called FQPSK-B, which was a patented version of FQPSK [17]. Subsequently efforts were made to reduce the complexity in implementation, which has resulted in a non-patented version, known as FQPSK-JR [18]. Later FQPSK-JR was introduced into IRIG-106 as candidate modulation method by RCC in 2004. Conceptually FQPSK-JR in the form of OQPSK modulation is defined as

$$S_{FQ}(t) = \sum_m s_{I,n}(t - mT_s) + js_{Q,n}(t - mT_s - T_s/2) \quad (1.24)$$

where $s_{I,n}(t)$ and $s_{Q,n}(t)$ are data dependent pulses which are selected in a constrained manner from a pool of 16 waveforms [18]. These 16 waveforms are defined for two bit intervals $2T_b = T_s$ [16, 18]. Simon's XTCQM interpretation has 16 waveforms each for I and Q components, making a total 32 possible waveforms. By incorporating the input data dependency, FQPSK-JR can be re-expressed in the following form

$$S_{FQ}(t) = \sum_m I_{FQ}(t - mT_s; a_{2m}, \dots, a_{2m-4}) + jQ_{FQ}(t - mT_s; a_{2m}, \dots, a_{2m-4}) \quad (1.25)$$

Five information bits ($a_{2m}, a_{2m-1}, a_{2m-2}, a_{2m-3}, a_{2m-4}$) are used for selecting in-phase $I_{FQ}(t)$ and quadrature $Q_{FQ}(t)$ waveforms during symbol transmission interval T_s . In the next symbol interval two new data bits are allowed while discarding the two oldest data bits which forms a new set of 5 bits. This new set of 5 data bits then selects the $I_{FQ}(t)$ and $Q_{FQ}(t)$ waveforms for the next symbol interval. This process acts as a five bit wide sliding window which moves for 2 input data bits at a time. This reflects the inherent memory in this modulation.

The phase pulse $q_{FQ}(t)$, to express the CPM approximation of FQPSK-JR [3] is derived from XTCQM representation. As the XTCQM waveforms are defined for 2 bit interval, the length of phase pulse $q_{FQ}(t)$ is $L = 2T_b$. The phase pulse for CPM approximation of FQPSK-JR is [3, 19]

$$q_{FQ}(t) = \arctan \left[\frac{-A \cos(\frac{\pi t}{2T_b})}{\sqrt{1 - A^2 \cos^2(\frac{\pi t}{2T_b})}} \right] \quad (1.26)$$

The frequency pulse $g_{FQ}(t)$ is evaluated by taking time derivative of phase pulse $q_{FQ}(t)$ as [3, 19]

$$g_{FQ}(t) = \frac{\frac{A\pi}{2T_b} \sin(\frac{\pi t}{2T_b})}{\sqrt{1 - A^2 \cos^2(\frac{\pi t}{2T_b})}} \quad (1.27)$$

where $A = 1/\sqrt{2}$ is chosen to make the envelope of the modulated wave constant. Fig. 1.7 shows the frequency and phase pulse to generate CPM approximation of FQPSK-JR.

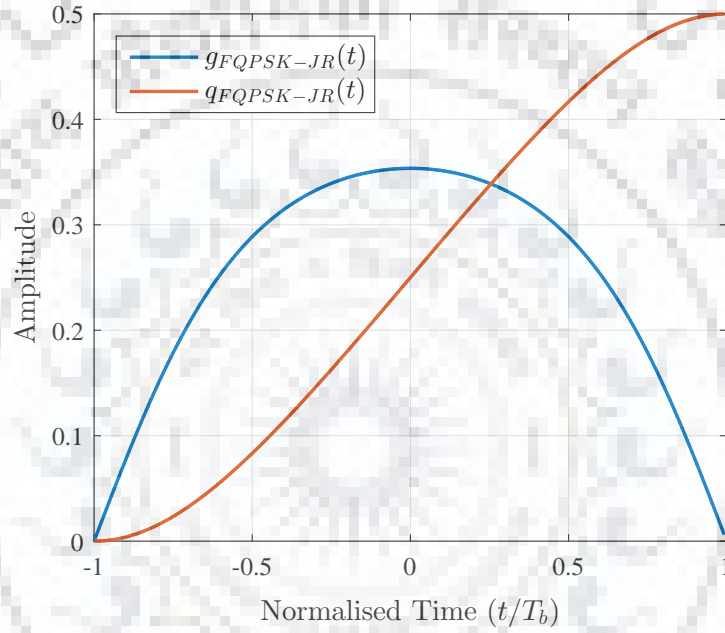


Fig. 1.7. Simulated frequency pulse $g(t)$ and phase pulse $q(t)$ for FQPSK-JR

1.3.3 ARTM-CPM

ARTM-CPM is a quaternary modulation method where instantaneous frequency of the modulated signal $s(t)$ is derived from the input bit sequence b_i . This is the most bandwidth efficient modulation scheme among all the tier II waveforms, however it lacks in detection efficiency as it suffers from higher reacquisition time (Table A-3 of Appendix A [6]). A block schematic of ARTM CPM modulator is illustrated in Fig. 1.8. This schematic appears to be same as that used for SOQPSK-TG, however in this case the phase of the CPM modulated signal is defined as [20]

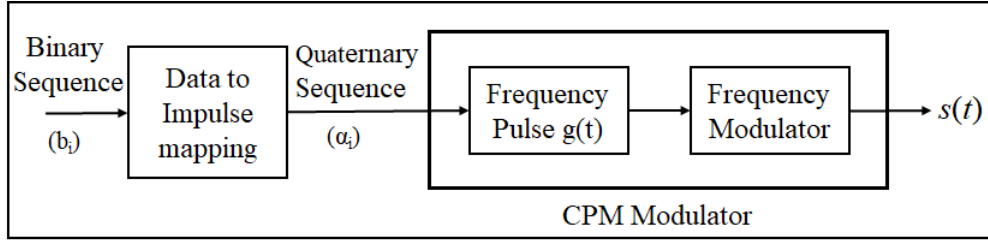


Fig. 1.8. Conceptual ARTM-CPM modulator

$$\phi(t, \alpha) = 2\pi \int_{-\infty}^t \sum_{i=-\infty}^{\infty} h_i \alpha_i g(\tau - iT_b) d\tau = 2\pi \sum_{i=-\infty}^{\infty} h_i \alpha_i q(t - iT_b) \quad (1.28)$$

where modulation index h_i alternates between h_1 and h_2 along with the symbol rate, where $h_1 = 4/16$ and $h_2 = 5/16$. The quaternary sequence α_i is generated from the binary sequence b_i as per the mapping method shown Table 1.2. The frequency pulse is a raised cosine function spreading across three symbol periods [6]

$$g_M(t) = \frac{1}{6T} \left[1 - \cos \left(\frac{2\pi t}{3T} \right) \right] \quad \text{for } 0 \leq t \leq 3T \quad (1.29)$$

where T denotes symbol period and is equal to $2T_b$. Fig. 1.9 illustrates the frequency pulse and phase pulse used to generate ARTM-CPM.

Table 1.2: Symbol mapping for ARTM-CPM [6]

Input Dibit [b(i)b(i + 1)]	Quaternary Alphabet [α_i]
11	+3
10	+1
01	-1
00	-3

In ARTM-CPM, superior spectral efficiency is achieved because of increased modulation order (quaternary scheme), usage of reduced modulation index and using a frequency pulse which is relatively smooth and spreads across 3 bit periods. On the other hand improved detection efficiency is achieved because of alternating modulation index between h_1 and h_2 . However due to this alternation between h_1 and h_2 , the receiver complexity increases many folds.

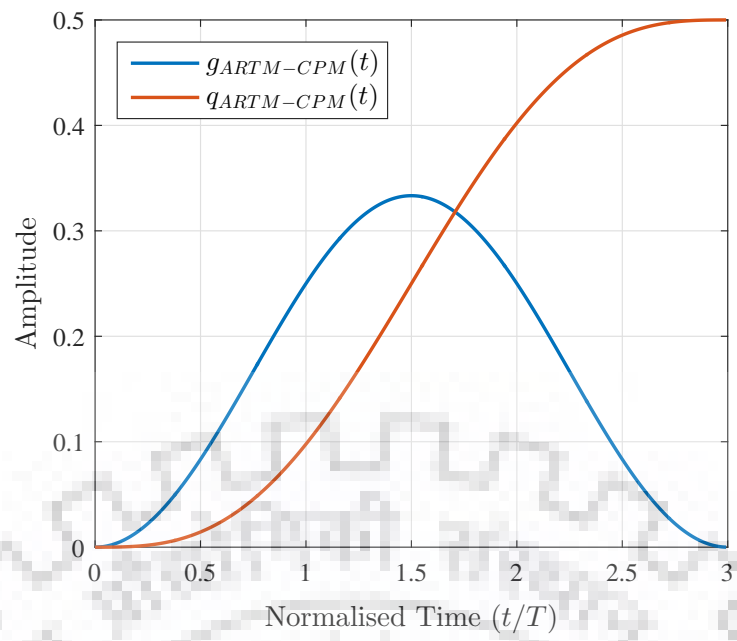


Fig. 1.9. Simulated frequency pulse $g(t)$ and phase pulse $q(t)$ for ARTM-CPM

Chapter 2

Literature Survey

In aeronautical telemetry measurements are made on aeronautical vehicle and those measurements are send to a distant location for performance analysis while ensuring flight safety. Generally two antennas (one at back another at belly) are installed on the aircraft to provide approximately omnidirectional data coverage. However sometimes Aircraft structure can obstruct transmission from any one of the antenna to the Telemetry station as shown in Fig. 2.1 [5,21]. The separation between antennas is usually of the order of several wavelengths (λ). Thus a small variation in the aircraft position creates large phase difference between the two received signals. When these received signals form two on-board antennas have equal magnitude and opposite phase, they will interfere with each other leading to signal cancellation termed as “two-antenna problem”.

To deal with this issue, signal transmission from each antenna can be achieved on two independent frequencies. This solution increases transmission bandwidth by two times. Considering the fact of increasing data rate requirement and the overcrowding of the allotted spectrum [22] this solution is not preferred. As an alternative, continuous antenna beam steering (considering both antennas as antenna array) can be performed to direct the signal towards telemetry station. This method is mechanically complex, and requires continuous update on the precise telemetry location with reference to aircraft. The third alternative is STC, which are used to increase the data transmission capacity in multiple input multiple output (MIMO) systems [23]. S. Alamouti [8] showed that STC can be used to implement the transmit diversity by using two transmit antenna. M. Jensen in their paper [2] showed that Alamouti encoded QPSK signal solves this self-interference problem.

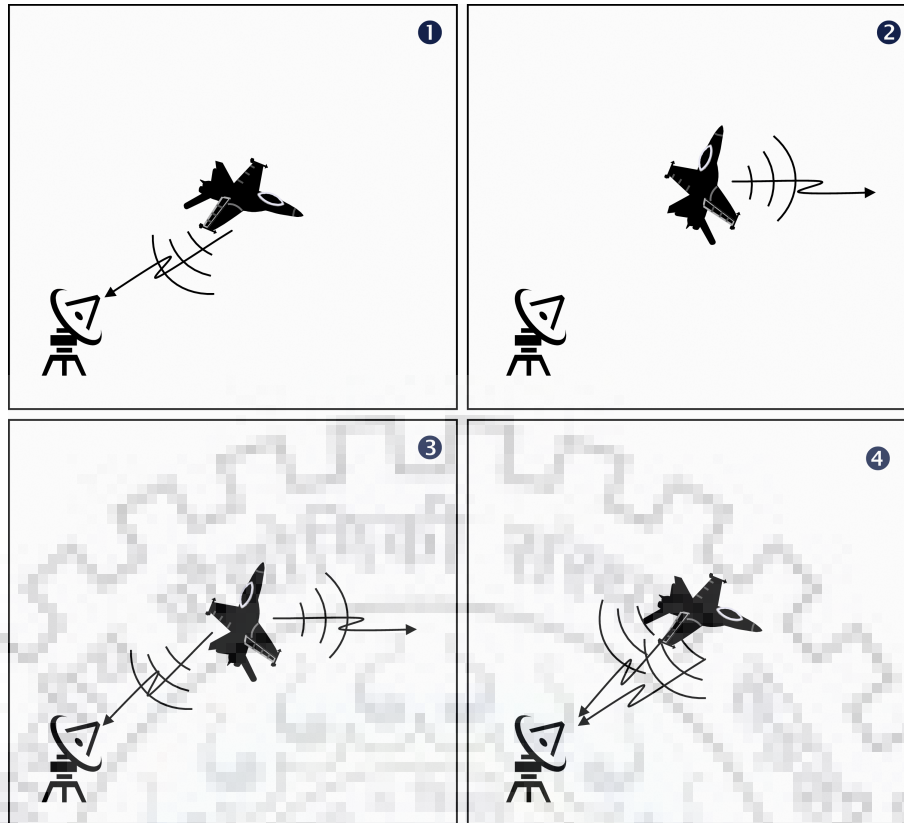


Fig. 2.1. Illustration of self interference due to transmission from two antennas [2]

To implement this idea to the aeronautical applications, several important issues need to be addressed

1. The modulation scheme used is SOQPSK-TG, which is defined in the IRIG-106 standard [6]. It is one of the CPM scheme [10,24–26] and its application to Alamouti code is not linear.
2. Signal from each antenna passes through two different channels whose impulse response is required by the receiving decoder. This can be estimated by using the periodically inserted pilot sequence in the transmitted stream.
3. The received signal gets effected by the frequency offset due to doppler shift and oscillator uncertainties. This also can be estimated by using pilot sequence.
4. Due to high bit rate (10 to 20 Mb/s) and large separations between two transmit antennas, received signal from each antenna undergoes different delays. These delays are also can be estimated by using pilot sequence.

In this thesis ML estimation for frequency offset, channel delays and channel gains is derived and analyzed. This problem is unique as the parallel channel undergoes different

delays. Since joint estimation is computationally complex and requires 3-Dimensional (3-D) search for its implementation, a sequential estimation based algorithm is derived and analyzed.

These estimated parameters are used by the space time decoder at the receiver to detect the transmitted bit pattern. As SOQPSK-TG is a partial response scheme, its trellis structure possess 512 waveform states. Detection by MLSE method requires search over two possible trellis (arises due to differential delays). Implementation of branch metric calculation for these many states is highly complex [4]. These waveform states can be reduced by limiting the frequency pulse duration, thus reducing decoder complexity. Pulse shaping has been proposed to generate the SOQPSK-TG approximation, which is subsequently used for the parameter estimation in STC encoded telemetry system. CPM approximation of EQPSK-JR has also been considered as another candidate for parameter estimation. The mean squared error (MSE) performances for both of these schemes are found to be satisfactory and meeting the CRB criteria.



Chapter 3

System Model for Estimation

This chapter provides information regarding Alamouti encoding of SOQPSK-TG. It demonstrates how SOQPSK-TG phase states are encoded using Alamouti STC. This chapter subsequently explains signal modeling while capturing the effect of frequency offset, channel gain and channel delays on the transmitted signal. It also elaborates about the frame synchronization procedure to capture the pilot samples in the received signal.

3.1 Alamouti-Encoding for SOQPSK-TG

As brought out in section 1.3.1, that SOQPSK-TG is a nonlinear CPM method. Thus, the application of SOQPSK-TG to the Alamouti codes is not as apparent as it might appear. Alamouti STC can be applied to SOQPSK-TG by encoding the CPM phase states. This way the benefits of Alamouti STC for SOQPSK-TG is achieved. To understand this, the phase of a SOQPSK-TG signal (1.20) can also be expressed as [24–26]

$$\phi(t; \alpha) = \frac{\pi}{2} \sum_{k=0}^{n-L} \alpha_k + \pi \sum_{k=n-L+1}^n \alpha_k q(t - kT_b) \quad (3.1)$$

To the right side of (3.1) the first term corresponds to the phase states and the second term corresponds to the correlative states. SOQPSK-TG has four phase states

$$\theta_{n-L} = \left\{ 0, \frac{\pi}{2}, \pi, \frac{3\pi}{2} \right\} \quad (3.2)$$

and 2^{L-1} correlative states. These phase states and correlative states together produce 512 waveform states. The relationship between pairs of input bits (Trellis state variable defined by S_n) and CPM phase states θ_{n-L} is illustrated in Fig. 3.1.

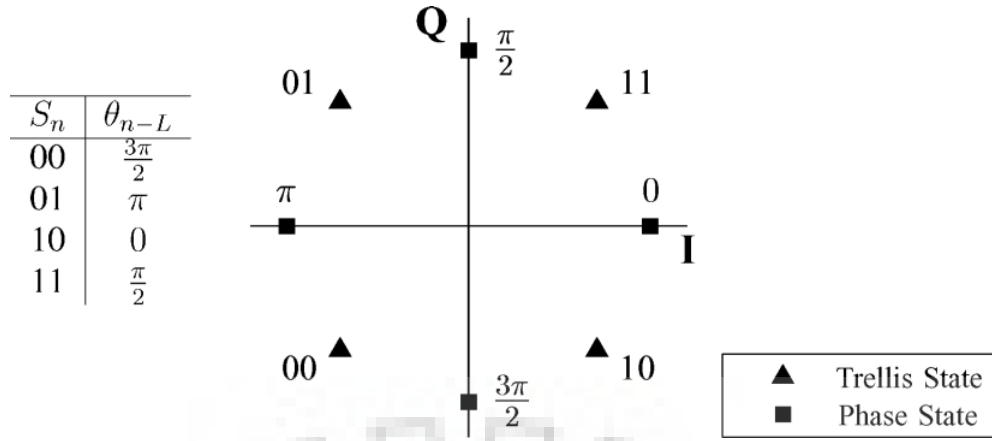


Fig. 3.1. Relation between phase states and trellis states [3]

These phase states are used by SOQPSK-TG Alamouti encoder as illustrated in Fig. 3.2. The I/Q plot illustrates the four-state approximation in which the labels are taken from Fig. M-2 of IRIG-106 [6]. The table beside I/Q plot summarizes the Alamouti STC in terms of complex symbols and their equivalent bit level code.

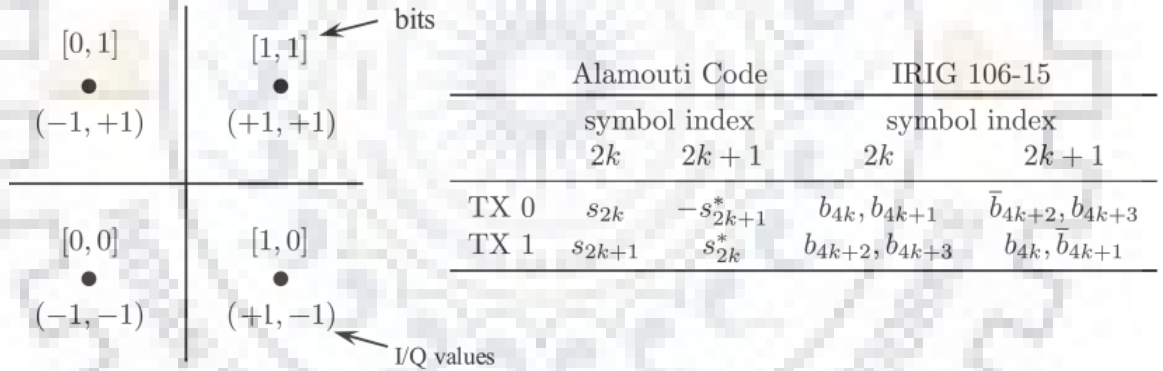


Fig. 3.2. Relation between SOQPSK-TG four-state approximation, Alamouti STC and bit-level equivalent encoder [4]

The bit-level encoding presented in table defines a “bit-level Alamouti encoder” for SOQPSK-TG, which is shown in Fig. 3.3. The bit-level STC generates two parallel binary streams that are applied to separate SOQPSK-TG modulators.

The input bit stream \mathbf{b} is expressed as

$$\mathbf{b} = [b_0 \ b_1 \ b_2 \ b_3 \ \cdots \ b_{4k} \ b_{4k+1} \ b_{4k+2} \ b_{4k+3} \ \cdots] \quad (3.3)$$

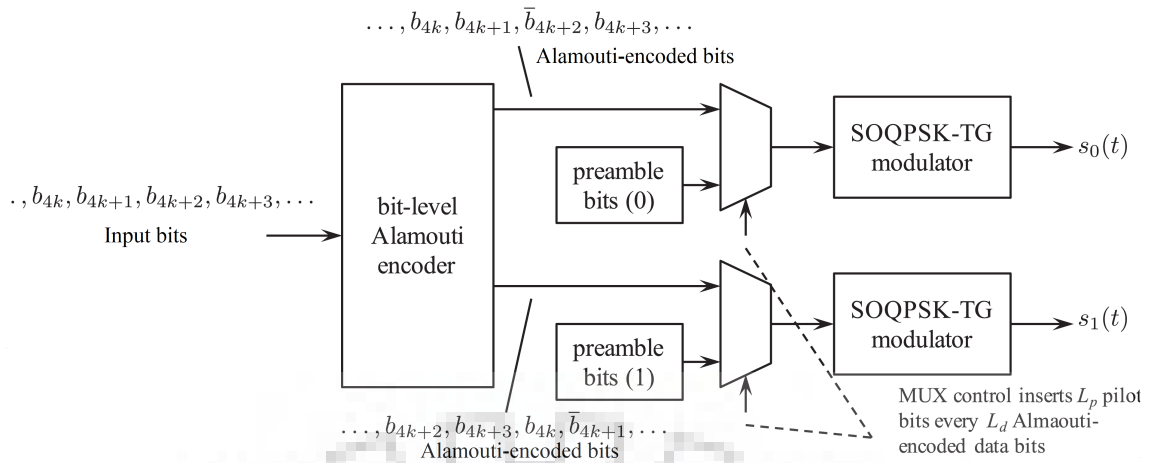


Fig. 3.3. Alamouti encoding for SOQPSK-TG [5]

The “bit-level Alamouti encoder” arranges this input bit stream \mathbf{b} into two bit streams consisting blocks of 4 bit length [4, 21]

$$\mathbf{b}^{(0)} = [b_0 \ b_1 \ \bar{b}_2 \ b_3 \ \dots \ b_{4k} \ b_{4k+1} \ \bar{b}_{4k+2} \ b_{4k+3} \ \dots] \quad (3.4)$$

$$\mathbf{b}^{(1)} = [b_2 \ b_3 \ b_0 \ \bar{b}_1 \ \dots \ b_{4k+2} \ b_{4k+3} \ b_{4k} \ \bar{b}_{4k+1} \ \dots] \quad (3.5)$$

These two bit streams are then multiplexed with respective pilot sequences to make two parallel frames as per frame structure shown in Fig. 3.4. Subsequently these two parallel frames are then fed to separate SOQPSK-TG modulators.

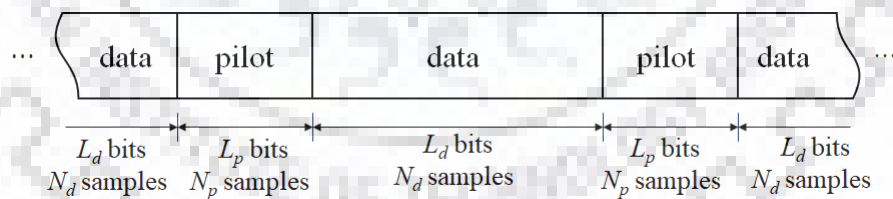


Fig. 3.4. Frame structure

3.2 Signal Modeling

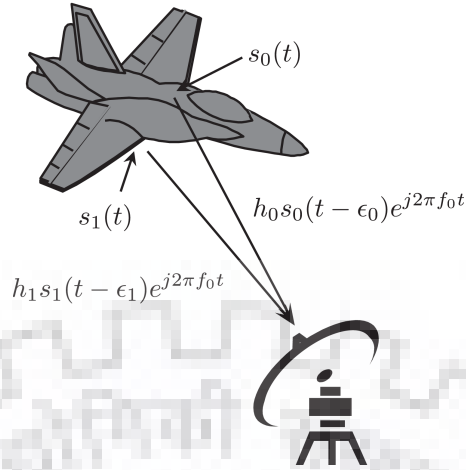


Fig. 3.5. Transmission from aircraft to telemetry station [5]

Using Alamouti STC as explained in previous section, two modulated signals $s_0(t)$ and $s_1(t)$ are simultaneously transmitted from the top and bottom antennas. Both of these signals undergoes a complex-valued channel attenuation of h_0 and h_1 respectively and time delay of ϵ_0 sec and ϵ_1 sec respectively. The signal received at the Telemetry station is expressed as [5]

$$r(t) = \left[h_0 s_0(t - \epsilon_0) + h_1 s_1(t - \epsilon_1) \right] e^{j2\pi f_0 t} + z(t) \quad (3.6)$$

where f_0 is frequency offset in cycles/s and $z(t)$ is complex-valued random process representing white gaussian thermal noise with zero-mean and PSD of $2N_0$. The sampled received signal at the output of anti-aliasing low pass filter is expressed as

$$r(nT) = \left[h_0 s_0((n - \tau_0)T) + h_1 s_1((n - \tau_1)T) \right] e^{j\omega_0 n} + w(nT) \quad (3.7)$$

where $\omega_0 = 2\pi f_0 T$ rads/sample represents frequency offset in discrete-time domain, $\tau_0 = \epsilon_0/T$ and $\tau_1 = \epsilon_1/T$ are timing delays with reference to the sampling time, and $w(nT)$ are samples obtained after filtering and sampling $z(t)$. Let us consider that the antialiasing filter is an ideal low pass filter having bandwidth of $1/2T$, then noise samples $w(nT)$ are iid complex-valued Gaussian random variables having zero mean and variance of $2\sigma^2 = 2N_0/T$. The sampling rate is chosen to be integer multiple of data rate as

$$\frac{T_b}{T} = N \quad \text{samples/bit.} \quad (3.8)$$

Our aim is estimation of unknown parameters h_0 , h_1 , τ_0 , τ_1 and ω_0 from the received signal samples $r(nT)$. To carry out estimation of these unknown parameters, pilot sequences $p_0(nT_b)$ and $p_1(nT_b)$ are individually multiplexed with two parallel Alamouti encoded bit streams, which are subsequently passed through the respective SOQPSK-TG modulators. These two modulated signals are transmitted by two on-board antennas as illustrated in Fig. 3.3 and Fig. 3.5.

3.3 Frame Synchronization

The frame formatting is obtained by periodically placing L_p pilot bits before every L_d Alamouti-encoded data bits as shown in Fig. 3.4. As the sampling rate is chosen at $N = 4$ sample/bit, $N_p = N \times L_p$ SOQPSK-TG modulated pilot samples occurs before every $N_d = N \times L_d$ Alamouti-encoded SOQPSK-TG data samples. In terms of indexing SOQPSK-TG modulated samples for pilot bits starts at index $n = 0$ and are denoted as $p_0(nT)$ and $p_1(nT)$ for $n = 0, 1, \dots, (N_p - 1)$. Thus (3.7) becomes

$$r(nT) = \left[h_0 p_0((n - \tau_0)T) + h_1 p_1((n - \tau_1)T) \right] e^{j\omega_0 n} + w(nT) \quad (3.9)$$

for $n = 0, 1, \dots, (N_p - 1)$

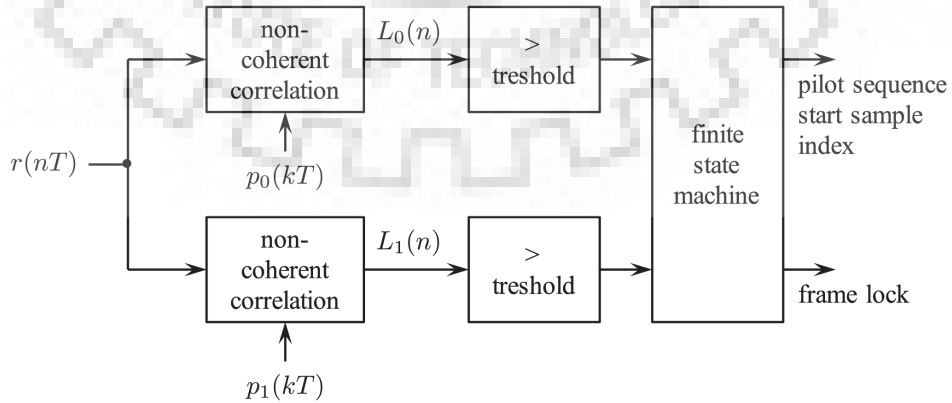


Fig. 3.6. Non-coherent frame synchronizer for detecting start of pilot sequence [5]

Frame synchronizers are generally used for the time synchronization of the incoming received data. This task is accomplished by identifying the beginning of the pilot sequence in the received signal samples $r(nT)$. To detect the beginning of pilot sequence, the received samples are correlated with copies of $p_0(kT)$ and $p_1(kT)$ which are locally stored at the receiver [27]. This same approach is followed by optimum frame synchronizer to deal with unknown frequency offsets, channel gains and channel delays, as explained in [27]. A simple method which is inspired by the frame synchronizer outlined in [28], is shown in Fig. 3.6, where correlation functions are defined as [5]

$$\begin{aligned} L_0(n) &= \left| \sum_{k=0}^{N_p-1} r((k+n)T) p_0^*(kT) \right|^2 \\ L_1(n) &= \left| \sum_{k=0}^{N_p-1} r((k+n)T) p_1^*(kT) \right|^2 \end{aligned} \quad (3.10)$$

The received sequence $r(nT)$ is correlated (via non coherent correlators) in parallel branches with the locally stored copies of two pilot sequences $p_0(kT)$ and $p_1(kT)$. The frame lock is established by the finite state machine block. To obtain frame lock, state machine block look for three consecutive correlation peaks of either $L_0(n)$ or $L_1(n)$ with the correct separation distance. After identifying the start of the either pilot sequence, the detected sample index is used by the estimators to create $N_p \times 1$ vector \mathbf{r} .

Chapter 4

Parameter Estimation for SOQPSK-TG

This chapter provides insight into the estimation of five unknown parameters (h_0 , h_1 , τ_0 , τ_1 and ω_0), which are encountered during STC encoded telemetry data transmission from two on-board antennas. In section 4.1, ML estimation of frequency offset (ω_0), channel gains (h_0 and h_1) and time delays (τ_0 and τ_1) is derived and analyzed. Then, in section 4.2 and 4.3, two different schemes namely joint and sequential are explained for the ML estimation of these parameters. In the last section simulation results are presented for both the estimation schemes.

4.1 ML Estimation of Frequency Offset, Timing Delays and Channel Gains

The pilot samples, which are collected at the output of the frame synchronizer are arranged into a vector \mathbf{r} of size $Np \times 1$. This received vector \mathbf{r} in the form of matrix-vector equation is defined as

$$\mathbf{r} = \mathbf{\Omega P h} + \mathbf{w} \quad (4.1)$$

where \mathbf{h} represents 2×1 channel vector

$$\mathbf{h} = \begin{bmatrix} h_0 \\ h_1 \end{bmatrix} \quad (4.2)$$

$\mathbf{\Omega}$ represents $N_p \times N_p$ frequency offset matrix

$$\mathbf{\Omega} = \begin{bmatrix} 1 & & & \\ & e^{j\omega_0} & & \\ & & \ddots & \\ & & & e^{j(N-1)\omega_0} \end{bmatrix} \quad (4.3)$$

\mathbf{P} represents $N_p \times 2$ delay matrix

$$\mathbf{P} = \begin{bmatrix} p_0(-\tau_0 T) & p_1(-\tau_1 T) \\ p_0((1 - \tau_0)T) & p_1((1 - \tau_1)T) \\ \vdots & \vdots \\ p_0((N_p - 1 - \tau_0)T) & p_1((N_p - 1 - \tau_1)T) \end{bmatrix} \quad (4.4)$$

and \mathbf{w} represents $N_p \times 1$ vector of iid complex-valued Gaussian random variables representing AWGN noise

$$\mathbf{w} = \begin{bmatrix} w(0) \\ w(T) \\ \vdots \\ w((N_p - 1)T) \end{bmatrix} \quad (4.5)$$

The delay matrix \mathbf{P} is a function of the delay parameters defined in vector form as

$$\boldsymbol{\tau} = \begin{bmatrix} \tau_0 \\ \tau_1 \end{bmatrix} \quad (4.6)$$

As $w(nT)$ are samples of iid complex-valued circularly symmetric gaussian random variables whose mean is zero and variance is $2\sigma^2$, the conditional PDF of received vector \mathbf{r} is defined as [5]

$$f(\mathbf{r}|h_0, h_1, \tau_0, \tau_1, \omega_0) = \frac{1}{(2\pi\sigma^2)^{N_p}} \exp \left\{ -\frac{1}{2\sigma^2} |\mathbf{r} - \mathbf{\Omega P h}|^2 \right\}$$

4.2 Joint Estimator

By using the conditional probability density function $f(\mathbf{r}|h_0, h_1, \tau_0, \tau_1, \omega_0)$ of received vector \mathbf{r} the joint estimation of frequency offset, channel gains and channel delays is expressed as [5, 21]

$$\hat{\boldsymbol{\tau}}, \hat{\omega}_0 = \underset{\boldsymbol{\tau}, \omega_0}{\operatorname{argmin}} \left\{ \left| \left[\mathbf{I}_{N_p} - \boldsymbol{\Omega} \mathbf{P} (\mathbf{P}^H \mathbf{P})^{-1} \mathbf{P}^H \boldsymbol{\Omega}^H \right] \mathbf{r} \right|^2 \right\} \quad (4.7a)$$

$$\hat{\mathbf{h}} = \left(\hat{\mathbf{P}}^H \hat{\mathbf{P}} \right)^{-1} \hat{\mathbf{P}}^H \hat{\boldsymbol{\Omega}}^H \mathbf{r} \quad (4.7b)$$

where $\hat{\mathbf{P}}$ is evaluated as per (4.4) by using $\hat{\boldsymbol{\tau}} = \left[\hat{\tau}_0 \quad \hat{\tau}_1 \right]^T$ and $\hat{\boldsymbol{\Omega}}$ is evaluated from $\hat{\omega}_0$ in a similar fashion as $\boldsymbol{\Omega}$ is evaluated from ω_0 . This estimator functions in two steps. Delay and frequency offset are simultaneously estimated in the first step. The next step uses estimates of previous step for estimating channel gains. This estimator is computationally exhaustive as the initial step (4.7a) needs a 3-D search (simultaneous search for τ_0, τ_1 and ω_0). Thus a less complex estimation algorithm is required which is briefed in the next section.

4.3 Sequential Estimator

A less complex method is developed in this section to deal with the higher computational complexity encountered in joint estimator. This method is a simple sequential approach which is based on 2 dimensional search. This algorithm gets executed frame-by-frame basis as described follows. First estimation of frequency offset for the m^{th} frame is carried out by using the received pilot samples of the m^{th} frame. This estimation uses the channel gain and timing delay estimates from the $(m-1)^{th}$ frame. The estimated frequency offset from the m^{th} frame is subsequently used to de-rotate the received pilot samples of m^{th} frame. In the next step the timing delays for the m^{th} frame is estimated from the de-rotated pilot samples. Finally channel gains for the m^{th} frame are estimated from de-rotated pilot samples by using timing delay estimates. This algorithm is expressed in the mathematical form as follows [5]

$$\hat{\omega}_{0,m} = \underset{\omega_0}{\operatorname{argmax}} \left\{ \left| \hat{\mathbf{h}}_{m-1}^H \hat{\mathbf{P}}_{m-1}^H \boldsymbol{\Omega}^H \mathbf{r}_m \right|^2 \right\} \quad (4.8a)$$

$$\tilde{\mathbf{r}}_m = \hat{\boldsymbol{\Omega}}_m^H \mathbf{r}_m \quad (4.8b)$$

$$\hat{\tau}_m = \underset{\tau}{\operatorname{argmin}} \left\{ \left| \left[\mathbf{I}_{N_p} - \mathbf{P} (\mathbf{P}^H \mathbf{P})^{-1} \mathbf{P}^H \right] \tilde{\mathbf{r}}_m \right|^2 \right\} \quad (4.8c)$$

$$\hat{\mathbf{h}}_m = \left(\hat{\mathbf{P}}_m^H \hat{\mathbf{P}}_m \right)^{-1} \hat{\mathbf{P}}_m^H \tilde{\mathbf{r}}_m \quad (4.8d)$$

for $m = 1, 2, \dots$ (m indicates frame index). To initialize the algorithm following vector initialization can be considered

$$\hat{\tau}_0 = \begin{bmatrix} 0 \\ 0 \end{bmatrix} \quad \hat{\mathbf{h}}_0 = \begin{bmatrix} 1/\sqrt{2} \\ 1/\sqrt{2} \end{bmatrix} \quad (4.9)$$

The implementation considerations for the (4.8) are brought out in [5].

4.4 Performance Metric

For both the estimation algorithms, estimation errors are calculated to find the estimation error variances. The consolidated channel estimator error variance is expressed as channel error variance defined below

$$\text{Channel error variance} = \mathbb{E} \left\{ \left| h_0 - \hat{h}_0 \right|^2 \right\} + \mathbb{E} \left\{ \left| h_1 - \hat{h}_1 \right|^2 \right\} \quad (4.10)$$

Similarly consolidated delay estimator error variance is defined as

$$\text{Timing error variance} = \mathbb{E} \left\{ (\tau_0 - \hat{\tau}_0)^2 \right\} + \mathbb{E} \left\{ (\tau_1 - \hat{\tau}_1)^2 \right\} \quad (4.11)$$

and frequency offset error variance is defined as

$$\text{Frequency offset error variance} = \mathbb{E} \left\{ (\omega_0 - \hat{\omega}_0)^2 \right\} \quad (4.12)$$

4.5 Simulation Results

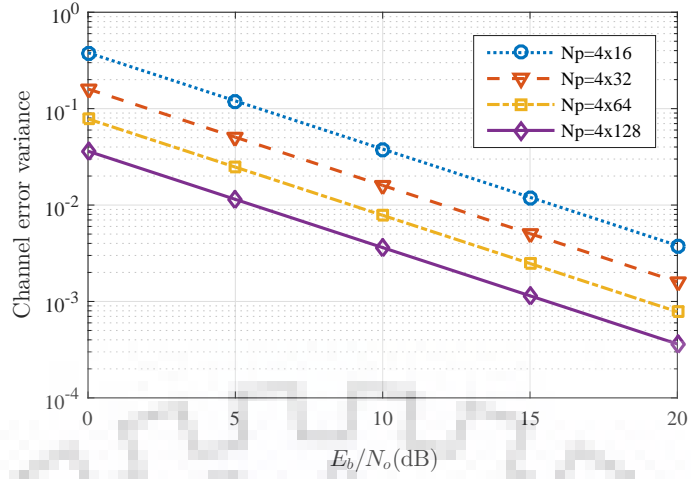
Pilot bits were periodically inserted in the input data stream for estimating the frequency offset (ω_0), the time delays (τ_0 and τ_1) and the channel gains (h_0 and h_1). The simulation of estimation for these three unknown parameters by joint and sequential ML estimation methods was carried out based on the following simulation parameters:

1. All the estimator were operated on the SOQPSK-TG modulated signal, which was sampled at $N = 4$ samples/bit.
2. A fixed time delays of $\epsilon_0 = -0.125T_b$ and $\epsilon_1 = 0.20T_b$ were applied to the transmitted signals $s_0(t)$ and $s_1(t)$ respectively, where T_b represents bit period. These delays gets translated into the sample delays of $\tau_0 = -0.5$ and $\tau_1 = 0.8$ for the transmitted signal samples $s_0(nT)$ and $s_1(nT)$ respectively (by considering $N = 4$).

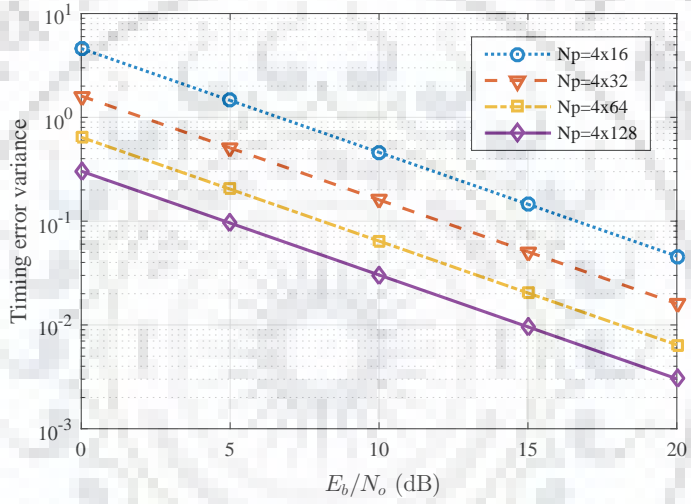
Table 4.1: Pilot sequences $p_0(nT_b)$ and $p_1(nT_b)$ of various length

Pilot length (L_p bits)	First pilot sequence $p_0(nT_b)$ (in Hex)
16	8207
32	ED70840F
64	818C5919BB0E881F
128	D99A4C31EEDDC1F811BB185223997B3F
Pilot length (L_p bits)	Second pilot sequence $p_1(nT_b)$ (in Hex)
16	080F
32	92519343
64	8C46E6771C5E943F
128	05B9DCE56B309B0CFE54B3A24EDA003E

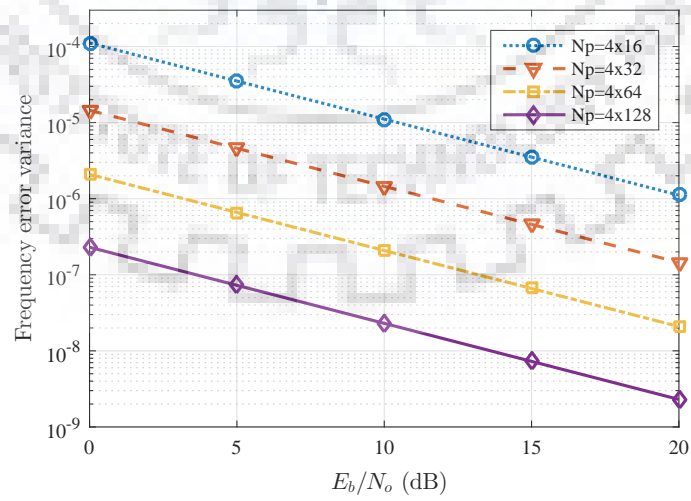
3. Pilot bits $p_0(nT_b)$ and $p_1(nT_b)$ were chosen to be pseudo-orthogonal bit pattern of varying size. Table 4.1 illustrates the different pilot pattern (in Hexadecimal format) for increasing pilot length L_p of 16, 32, 64 and 128 bits.
4. A fixed channel gain pair $h_0 = \sqrt{0.5}$ and $h_0 = j\sqrt{0.5}$ (for the transmitted signals $s_0(t)$ and $s_1(t)$ respectively) was considered for estimation.



(a) Channel error variance



(b) Timing error variance



(c) Frequency offset error variance

Fig. 4.1. Effect of varying pilot length on CRB. The length of pilot sequence is mentioned as $N_p = N \times L_p$ for $N = 4$

5. $L_d = 3200$ data bits were placed after every L_p pilot bits for encapsulating the data into frame before transmission.

The CRB (derived in Appendix A) for the estimation of unknown parameters is plotted in Fig. 4.1 for varying pilot length of 16, 32, 64, and 128-bits (selected from Table 4.1). In Fig. 4.1(a) the channel error variance, in Fig. 4.1(b) the timing error variance and in Fig. 4.1(c) the frequency offset error variance is illustrated. It is understood from the plots that the error performance for all the three parameters are getting improved with increasing pilot length.

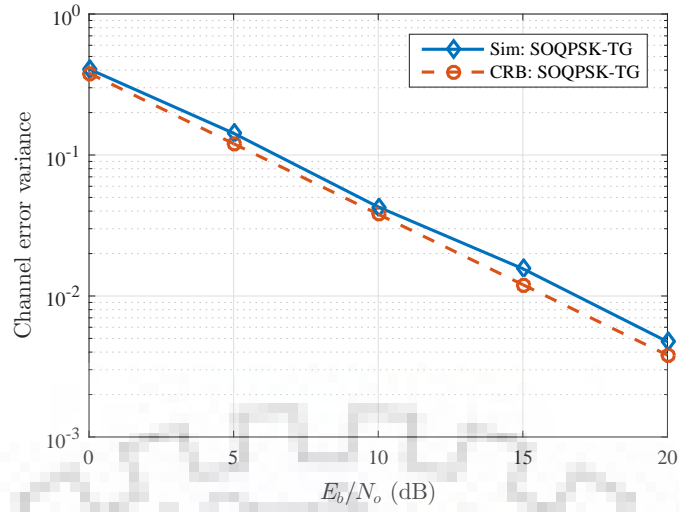
4.5.1 Joint Estimator

STC encoded bit streams were formatted by periodically inserting pilot pattern of $L_p = 16$ bits (Table 4.1), and data length of $L_d = 3200$ bits for each of the parallel streams. The modulated signal samples $s_0(nT)$ and $s_1(nT)$ underwent a channel attenuation of $h_0 = \sqrt{0.5}$ and $h_0 = j\sqrt{0.5}$, time delay of $\tau_0 = -0.5$ and $\tau_1 = 0.8$, and frequency offset of $\omega_0 = 2\pi \times 10^{-4}$. The pilot samples were captured in the received signal $r(nT)$ by frame synchronizer, and they were used by the estimator. The channel delays τ_0 and τ_1 were quantized to $Q * N$ parts per bit ($Q = 10$) in estimation process. Quantized values of τ (τ_0 and τ_1) and ω_0 were utilized for function minimization (4.7a) using brute force method. These frequency offset estimate ($\hat{\omega}_0$) and delay estimates ($\hat{\tau}_0$ and $\hat{\tau}_1$) were subsequently used in (4.7b). for channel gain estimation. The mean square error (MSE) for all the three parameters were evaluated over 100 experiments across multiple E_b/N_0 and are plotted in Fig. 4.2.

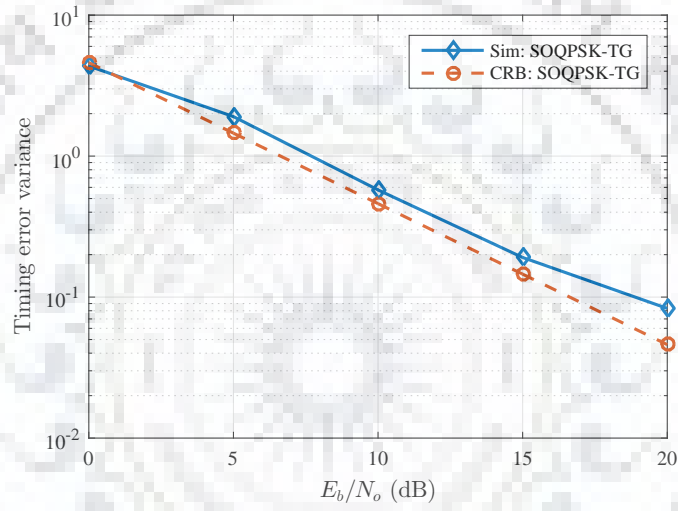
In Fig. 4.2(a), plotted channel error variance is the consolidated channel estimation error variance (4.10). Similarly in Fig. 4.2(b), plotted delay error variance is the consolidated delay estimation error variance (4.11). The MSE performance of all the three parameters are meeting the CRB criteria. However computational complexity of this estimator is enormous (due to 3-D search) which leads to higher simulation time.

4.5.2 Sequential Estimator

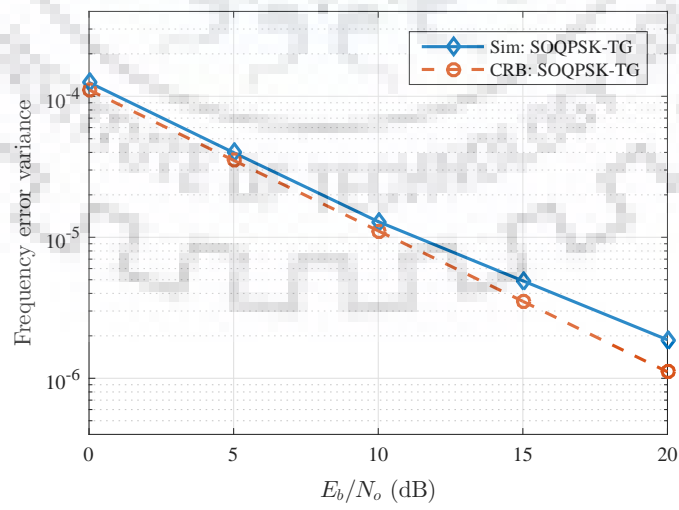
To deal with higher computational complexity encountered in joint estimator, simulation of sequential estimator (4.8) was carried out and plotted in Fig. 4.3. Frame formatting was carried out as in case of joint estimator, however in this case the pilot sequence of length $L_p = 64$ was chosen from Table 4.1.



(a) Channel error variance

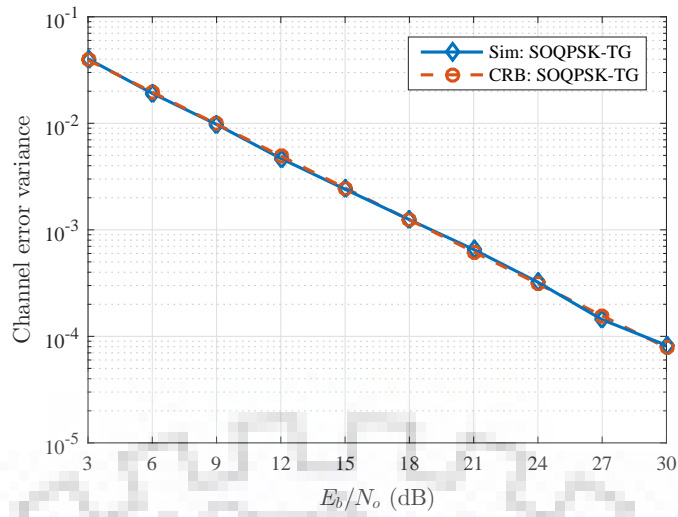


(b) Delay error variance

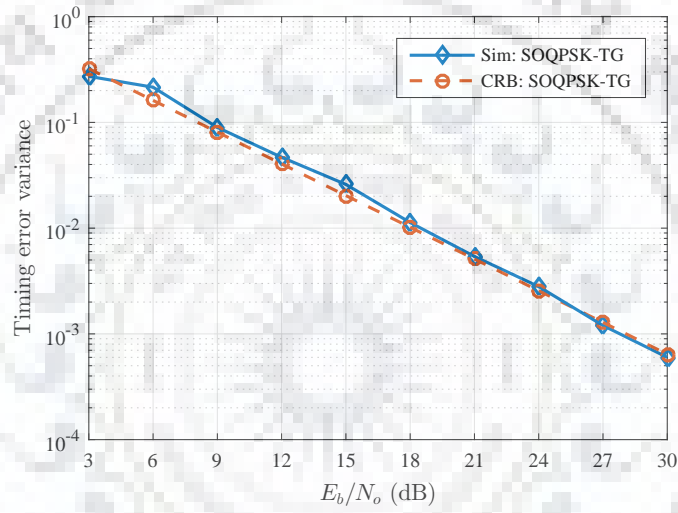


(c) Frequency offset error variance

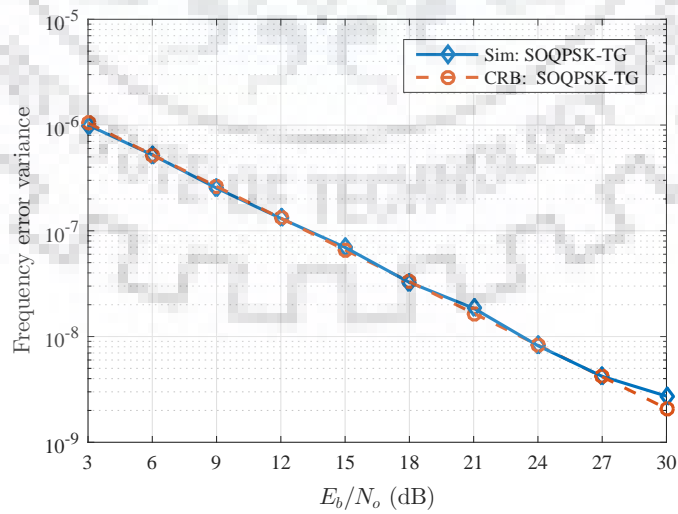
Fig. 4.2. Simulated MSE performance by using joint estimation method for pilot length $L_p = 16$ bits



(a) Channel error variance



(b) Delay error variance



(c) Frequency offset error variance

Fig. 4.3. Simulated MSE performance by using sequential estimation method for pilot length $L_p = 64$ bits

A fixed frequency offset of $\omega_0 = 2\pi \times 10^{-5}$ was incorporated in the signal samples undergoing channel attenuation of $h_0 = \sqrt{0.5}$ and $h_0 = j\sqrt{0.5}$, time delay of $\tau_0 = -0.5$ and $\tau_1 = 0.8$. In this case also channel delays τ_0 and τ_1 were searched from the quantized subspace of size $2 * Q * N$ ($Q = 10$ and $N = 4$) using brute force method. Simulated MSE performance by sequential estimation method are plotted in Fig. 4.3, which were evaluated over 250 frames for E_b/N_0 ranging from 3 to 30 dB. From Fig. 4.3 it is apparent that the MSE performance of all the three parameters are achieving the CRB for a wide range of SNR.



Chapter 5

Proposed work

In the previous chapter, simulated plots for the estimation of frequency offset (ω_0), time delays (τ_0 and τ_1) and channel gains (h_0 and h_1) by joint and sequential estimation methods were presented. It was shown that MSE performance is meeting the CRB criteria in both the cases. These estimations will be used by the Alamouti decoder at the receiver to detect the transmitted bits. Detection of this Alamouti encoded SOQPSK-TG signal by using MLSE require trellis search consisting 512 states. Due to these large number of states, branch metric computations is highly complex.

In this chapter, pulse shaping is carried out on the SOQPSK-TG frequency pulse to reduce the pulse length. Modulation generated by using this modified frequency pulse of length 2 (SOQPSK-2T) was selected to be the best available candidate in this process. Finally the MSE performance of STC encoded SOQPSK-2T by using sequential estimator was evaluated and compared with that of SOQPSK-TG . CPM approximation of FQPSK-JR was also chosen as one of the candidates in this comparison due to having close resemblance with SOQPSK-2T. By using SOQPSK-2T as modulation method, the Alamouti decoder complexity gets reduced because of lesser number of states (8 waveform states) in MLSE trellis structure.

5.1 Pulse shaping

To calculate the total number of states in MLSE detection of a CPM modulated signal, let us consider modulation index is defined as $h = n/p$, where n and p are relatively prime integers. Then the terminal phase states for a full response CPM waveform are expressed as [10]

$$\begin{aligned}\phi &= \left\{ 0, \frac{\pi n}{p}, \frac{2\pi n}{p}, \dots, \frac{(p-1)\pi n}{p} \right\}, & \text{for } n \text{ even} \\ \phi &= \left\{ 0, \frac{\pi n}{p}, \frac{2\pi n}{p}, \dots, \frac{(2p-1)\pi n}{p} \right\}, & \text{for } n \text{ odd}\end{aligned}\quad (5.1)$$

Thus when n is even the terminal phase states are p , but when n is odd the terminal phase states changes to $2p$. However in case of partial-response CPM (when frequency pulse extends over L symbol periods) the total number of phase states increases as expressed below

$$S = \begin{cases} pM^{L-1} & \text{even } n \\ 2pM^{L-1} & \text{odd } n \end{cases} \quad (5.2)$$

where M represents alphabet size. The modulation index and frequency pulse length in case of SOQPSK-TG are $h = 1/2$ and $L = 8$ respectively. Thus, in this case the total no. of states comes out to be 512 states, which is too high for branch metric calculation in trellis detector. Pulse shaping is proposed to shape the SOQPSK-TG frequency pulse by reducing the pulse length L , so that receiver complexity can be reduced. Three different pulse shapes of length $L = 6$, $L = 4$ and $L = 2$ are evaluated. The modified frequency pulse is proposed as

$$g(t) = C \frac{\cos\left(\frac{\pi\rho Bt}{2T_b}\right)}{1 - 4\left(\frac{\rho Bt}{2T_b}\right)^2} \times \frac{\sin\left(\frac{\pi Bt}{2T_b}\right)}{\left(\frac{\pi Bt}{2T_b}\right)} \times w_{LT}(t) \quad (5.3)$$

where, T_b , ρ and B has the same value as that in case of SOQPSK-TG, and $w_{LT}(T)$ is a time domain windowing function defined for variable pulse length L . To generate frequency pulse of length 6 bit intervals, $w_{6T}(T)$ can be defined as

$$w_{6T}(t) = \begin{cases} 1 & 0 \leq \left|\frac{t}{2T_b}\right| \leq T_1 \\ 0 & \left|\frac{t}{2T_b}\right| > T_1 \end{cases} \quad (5.4)$$

where, T_1 is same as that in case of SOQPSK-TG. Similarly, frequency pulse of length 4 bit intervals can be generated by $w_{4T}(T)$ as

$$w_{4T}(t) = \begin{cases} 1 & 0 \leq \left| \frac{t}{2T_b} \right| \leq \frac{2}{3}T_1 \\ 0 & \left| \frac{t}{2T_b} \right| > \frac{2}{3}T_1 \end{cases} \quad (5.5)$$

Likewise, windowing function $w_{2T}(T)$ for frequency pulse of length 2 bit intervals is defined as

$$w_{2T}(t) = \begin{cases} 1 & 0 \leq \left| \frac{t}{2T_b} \right| \leq \frac{1}{3}T_1 \\ 0 & \left| \frac{t}{2T_b} \right| > \frac{1}{3}T_1 \end{cases} \quad (5.6)$$

In all the three cases, the phase pulse is obtained by integrating the frequency pulse as

$$q(t) = \int_{-\infty}^t g(\tau) d\tau \quad (5.7)$$

The frequency and phase pulse for various modulations were simulated and pulse shaping was carried out on SOQPSK-TG frequency pulse as shown in Fig. 5.1. As brought out in chapter 1, FQPSK-JR is originally defined as XTCQM form, however its CPM approximation will have a frequency pulse of shape re-plotted in Fig. 5.1(b). SOQPSK-MIL is a full response variant of SOQPSK, and is defined for UHF satellite communication used in military applications (standard MIL-STD 188-181 [29]). It has a rectangular frequency pulse shape as plotted in Fig. 5.1(c). The frequency pulse of SOQPSK-TG is truncated to 6 symbol intervals (Fig. 5.1(d)) as the pulse is not varying for all the 8 symbol intervals. Similarly this truncation was carried out for a duration of 4 and 2 symbol intervals and plotted in Fig. 5.1(e) and Fig. 5.1(f) respectively. The phase pulse is also plotted along with the frequency pulse for all the cases.

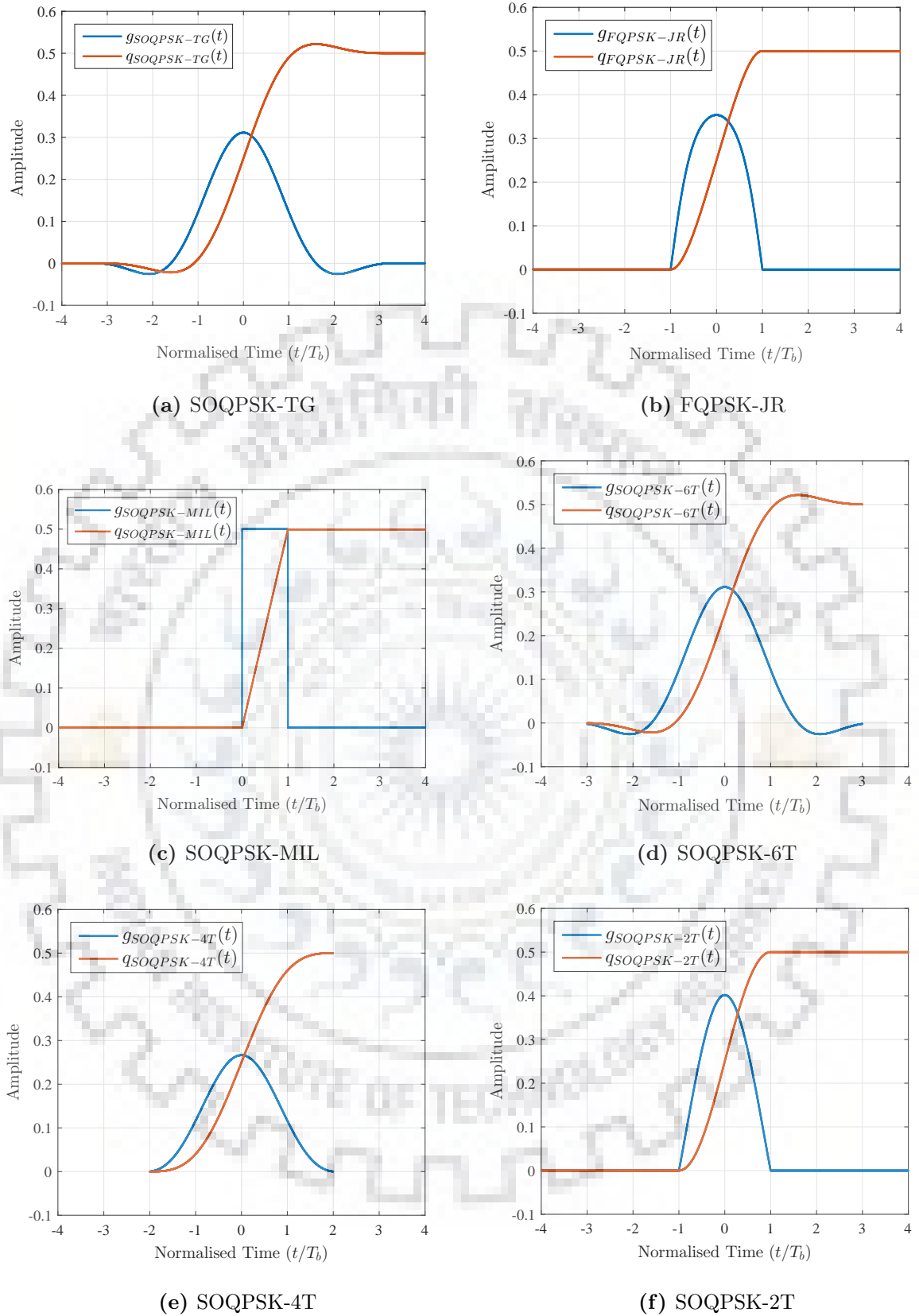


Fig. 5.1. Simulated frequency pulse $g(t)$ and phase pulse $q(t)$ for various modulations

5.2 Modulation Simulation

Simulation of various modulations was carried out by CPM method (1.19) by using various frequency pulses plotted in Fig. 5.1. Binary data was generated at 5 kbps and converted into ternary sequence by using (1.21) before applying to the CPM modulator. The complex valued samples generated at 2 samples per bit are plotted on the I-Q diagram as shown in Fig. 5.2 and phase trajectory are shown in Fig. 5.3. Both SOQPSK-TG and SOQPSK-6T has identical I-Q and phase trajectory plots, having constellation points clustered around 8 phase states. This clustering of the constellation points around 8 phases is seen for FQPSK-JR and SOQPSK-2T as well but with reduced no of points. Both FQPSK-JR and SOQPSK-2T have almost identical constellation distribution and phase trajectory. SOQPSK-MIL possess constellation points falling exactly at the 8 phase states because of which its phase trajectory is not as smooth as for other candidate waves. The I-Q plot of SOQPSK-4T has points which does not follow any pattern and are scattered all over the phase range of 2π . Due to this characteristic the detection of the SOQPSK-4T wave becomes extremely difficult as inherent offset modulation is lost in the constellation distribution.

Simulated power spectrum of various modulation schemes for a data generated at 5 kbps is shown in Fig. 5.4. The power spectrum of SOQPSK-6T is overlapping with that of SOQPSK-TG, which indicates that both the schemes occupies the same bandwidth. The power spectrum of SOQPSK-MIL shows that it possess multiple side lobes with wider bandwidth occupancy. Both FQPSK-JR and SOQPSK-2T have similar spectrum characteristic but SOQPSK-2T has relatively lower side lobe levels than FQPSK-JR. SOQPSK-4T has the narrowest spectrum among all the modulation candidates.

Table 5.1 summarizes 99% bandwidth vs receiver complexity comparison for various modulation simulations. From the table it is clear that SOQPSK-6T achieves exactly same bandwidth occupancy performance as that of SOQPSK-TG while reducing the number of states for MLSE detection by 4 times. SOQPSK-4T shows improved spectral efficiency than SOQPSK-TG while reducing the no. of states for MLSE detection to 32. Both SOQPSK-2T and FQPSK-JR requires 8 states for MLSE detection, however SOQPSK-2T occupies slightly more bandwidth than FQPSK-JR.

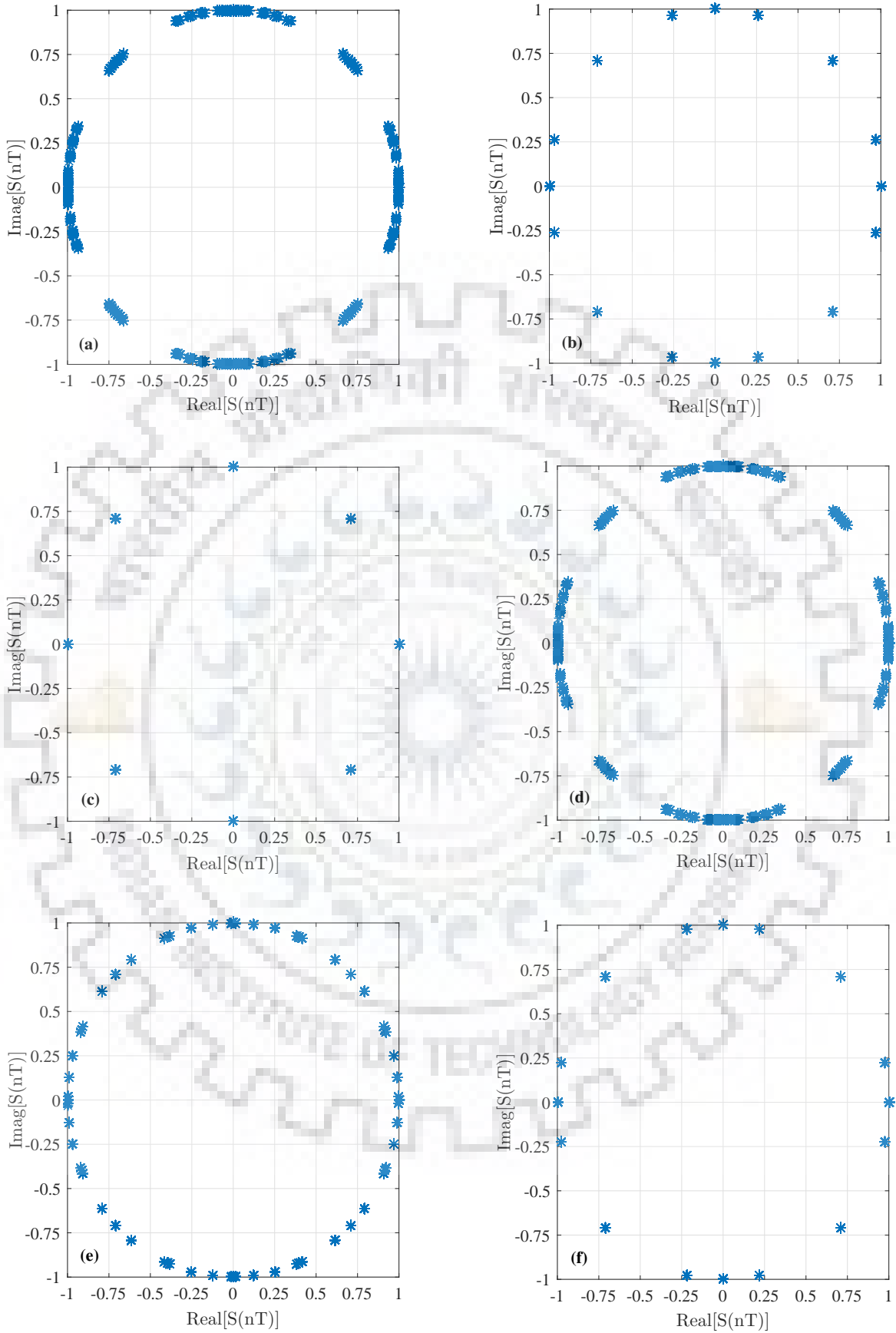


Fig. 5.2. Simulated complex valued samples for various modulations: (a) SOQPSK-TG; (b) FQPSK-JR; (c) SOQPSK-MIL; (d) SOQPSK-6T (Proposed); (e) SOQPSK-4T (Proposed); (f) SOQPSK-2T (Proposed)

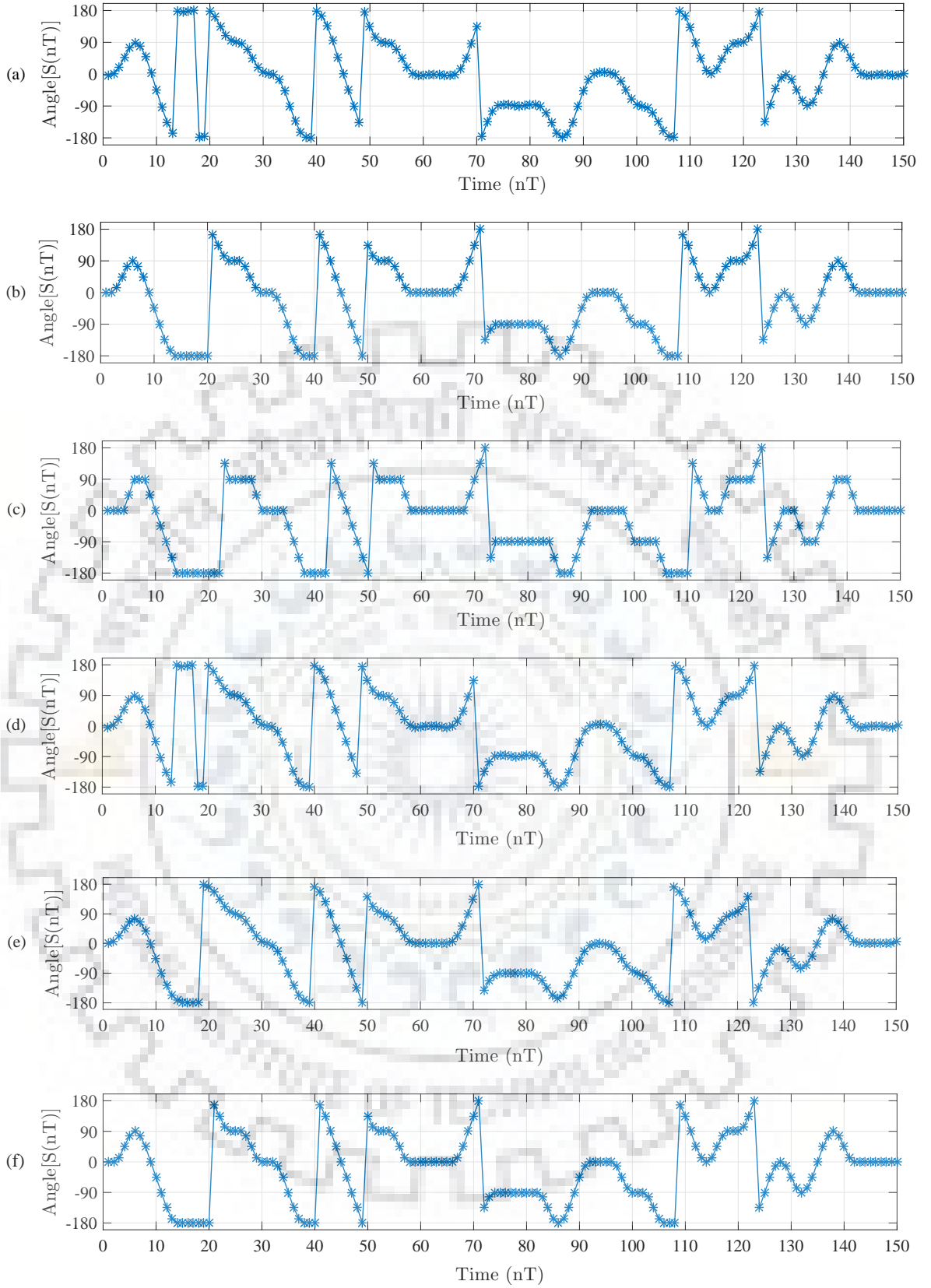


Fig. 5.3. Simulated phase trajectory for various modulations: (a) SOQPSK-TG; (b) FQPSK-JR; (c) SOQPSK-MIL; (d) SOQPSK-6T (Proposed); (e) SOQPSK-4T (Proposed); (f) SOQPSK-2T (Proposed)

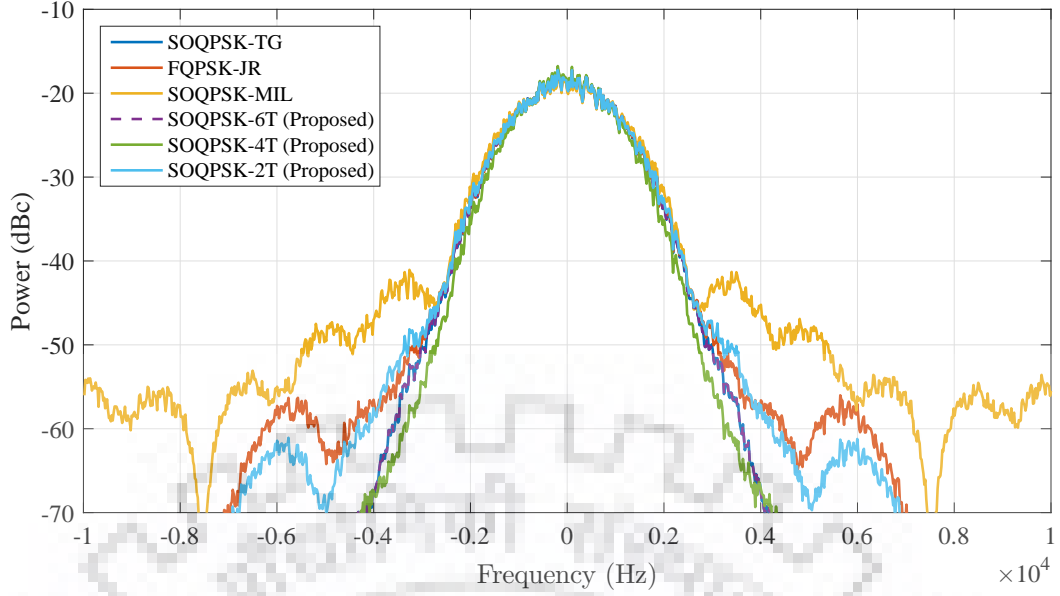


Fig. 5.4. Simulated power spectrum for various modulations at a data rate of 5 kbps

Table 5.1: Bandwidth occupancy vs Receiver complexity comparison for various modulation schemes

Modulation Type	Frequency Pulse Length (in bit Period)	99% Bandwidth	No. of states for MLSE detection
SOQPSK-TG	8	$\approx 0.78 * R_b$	512
FQPSK-JR	2	$\approx 0.79 * R_b$	8
SOQPSK-MIL	1	$\approx R_b$	4
SOQPSK-6T (Proposed)	6	$\approx 0.78 * R_b$	128
SOQPSK-4T (Proposed)	4	$\approx 0.74 * R_b$	32
SOQPSK-2T (Proposed)	2	$\approx 0.796 * R_b$	8

Considering the trade-off between receiver complexity and spectral occupancy, SOQPSK-2T is the best available candidate having 8 states for MLSE detection and bandwidth occupancy which is slightly more than that of SOQPSK-TG. Thus SOQPSK-2T will be STC encoded for parameter estimation by sequential estimation method. Along with SOQPSK-2T, FQPSK-JR will also be used by sequential estimator for MSE performance analysis, as they have almost similar characteristic as far as spectral occupancy and receiver complexity is concerned.

5.3 Parameter Estimation for STC encoded SOQPSK-2T and FQPSK-JR

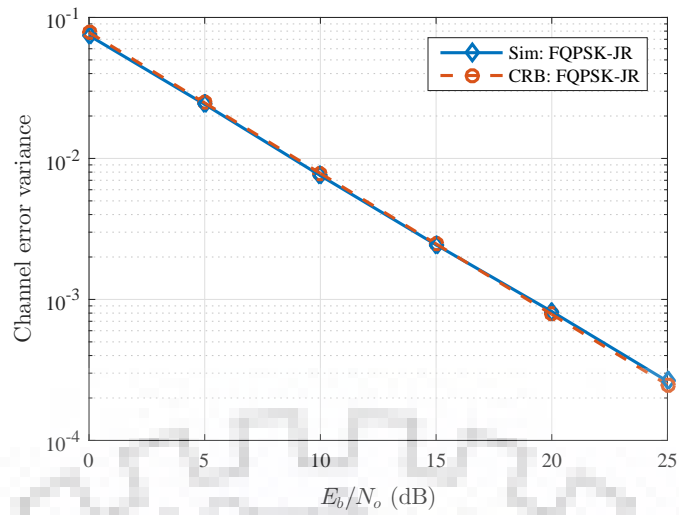
In this section SOQPSK-2T and FQPSK-JR will be separately considered for parameter estimation by sequential estimation method. The concept of bit level Alamouti encoding as brought out in section 3.1 will be applied to these two schemes as well. The two parallel frames, structured from the Alamouti encoded bits (as illustrated in Fig. 3.3 and Fig. 3.4) are fed to the respective modulator. The two parallel modulated signals $s_0(t)$ and $s_1(t)$ undergoes complex valued attenuation (h_0 and h_1), time delay (ϵ_0 and ϵ_1 seconds) and frequency offset f_0 Hz as expressed in (3.6). These channel impairments are estimated by the sequential estimator as per (4.8).

5.3.1 Simulation Results

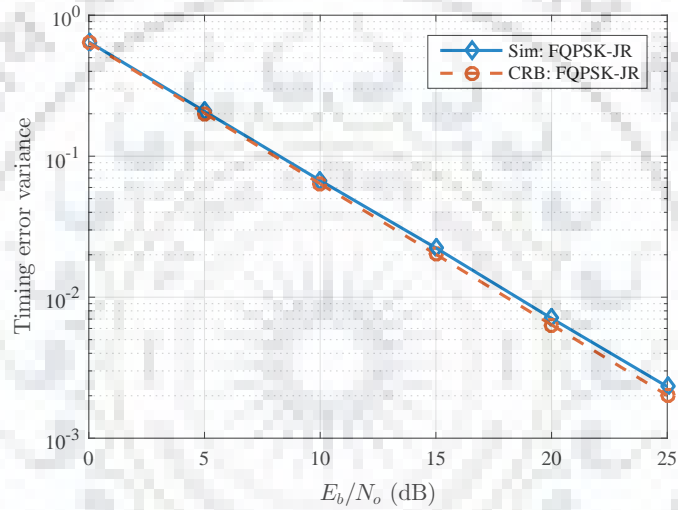
For the first case, pilot sequence of length $L_p = 64$ was chosen from Table 4.1 for estimation purpose. Modulated signal samples underwent a fixed frequency offset of $\omega_0 = 2\pi \times 10^{-5}$ rad/sec, channel attenuation of $h_0 = \sqrt{0.5}$ and $h_0 = j\sqrt{0.5}$ and normalized time delay of $\tau_0 = -0.5$ and $\tau_1 = 0.8$. These parameters were selected to emulate the situation when the reception at the telemetry station from the on-board antennas is of equal magnitude and opposite phase (Display Flight profile). The time delays τ_0 and τ_1 were searched from the quantized subspace of size $2QN$ ($-QN$ to QN for $Q = 10$ and $N = 4$) using brute force method for function minimization as per (4.8c).

Simulated mean squared errors for FQPSK-JR by sequential estimator are plotted in Fig. 5.5, which are evaluated over 250 frames for E_b/N_0 ranging from 0 to 25 dB. CRB is also plotted along with the respective MSE for all the three parameters. The overlapping of the MSE with CRB shows that estimation of all the parameters are achieving the CRB.

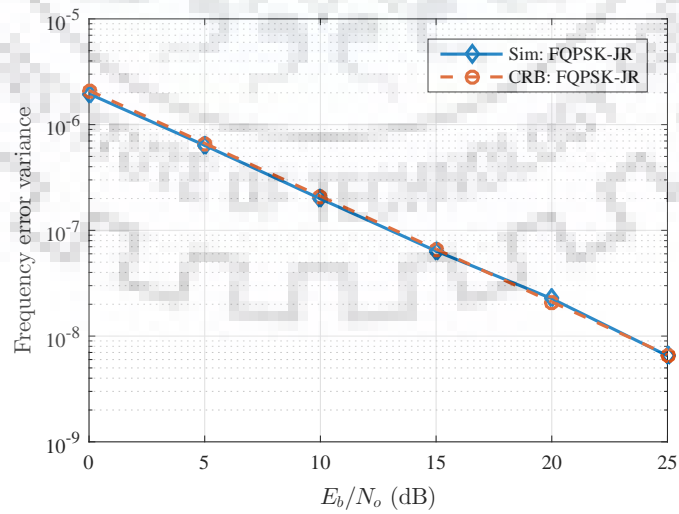
Simulation of SOQPSK-2T was carried out by taking the same simulation parameters as for FQPSK-JR. The simulated mean squared errors for this case are plotted in Fig. 5.6. For this case also the mean square errors were evaluated over 250 frames and E_b/N_0 ranging from 0 to 25 dB. Overlapping of the MSE plots with the respective CRB indicates that the estimated parameters are achieving the CRB.



(a) Channel error variance

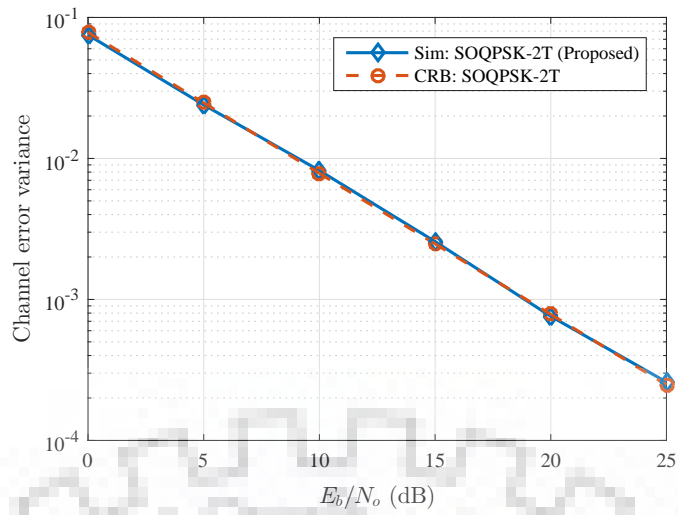


(b) Delay error variance

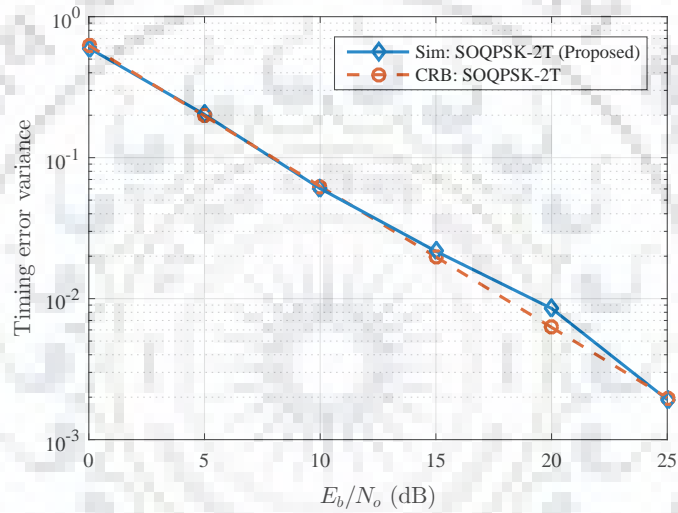


(c) Frequency offset error variance

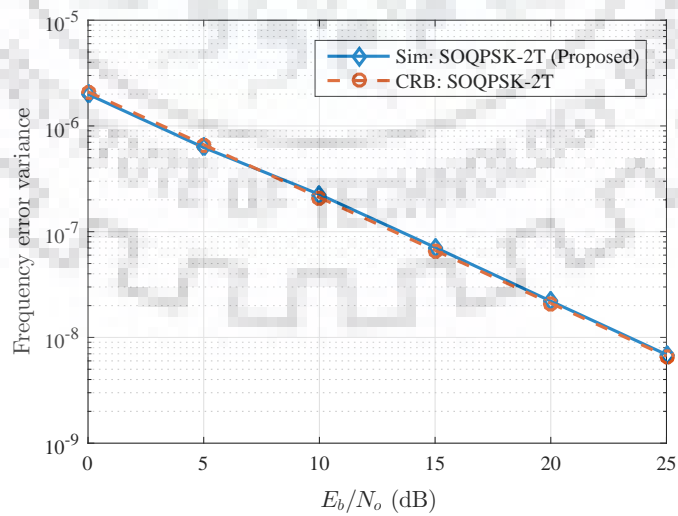
Fig. 5.5. Simulated MSE performance for FQPSK-JR by using sequential estimation method for display flight



(a) Channel error variance

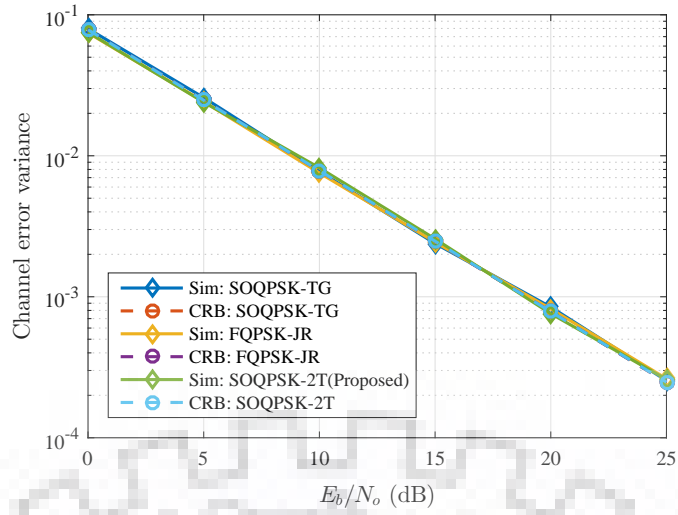


(b) Delay error variance

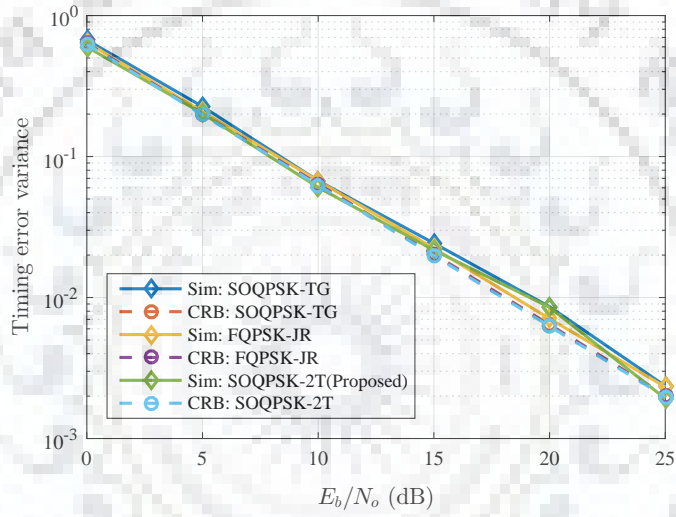


(c) Frequency offset error variance

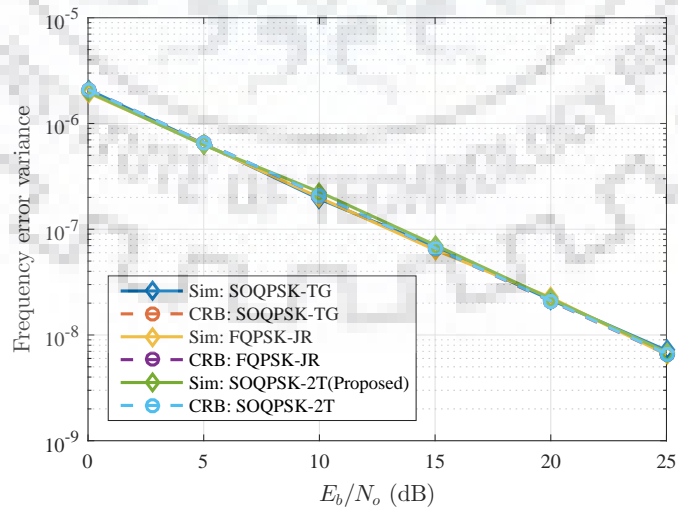
Fig. 5.6. Simulated MSE performance for SOQPSK-2T by using sequential estimation method for display flight



(a) Channel error variance



(b) Delay error variance

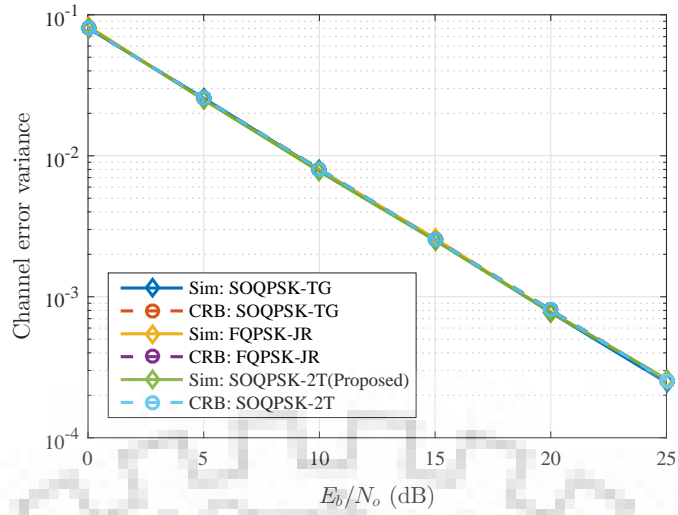


(c) Frequency offset error variance

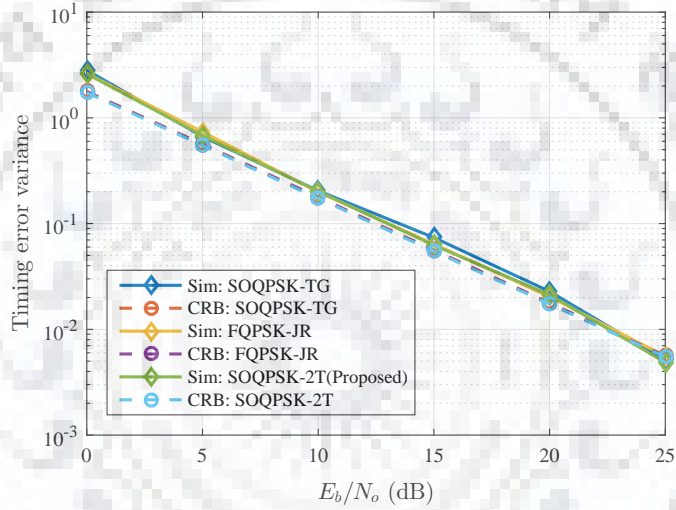
Fig. 5.7. Comparison of MSE performance for SOQPSK-TG, FQPSK-JR and SOQPSK-2T by using sequential estimation method for display flight

A comparative analysis of MSE performance was carried out between SOQPSK-TG, FQPSK-JR and SOQPSK-2T schemes. The simulated mean squared errors for all the three schemes by sequential estimator are plotted together in Fig. 5.7. The overlapping of all the plots shows that the mean square errors are same for all the three schemes and they are achieving the CRB.

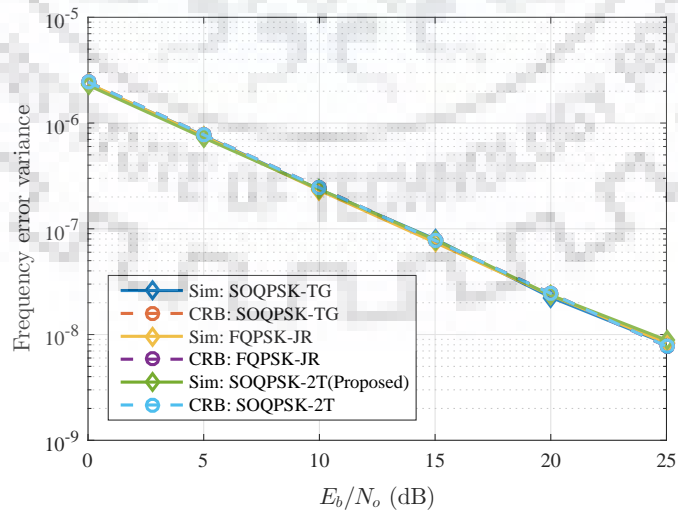
For the second case, unknown parameters were chosen to imitate the level flight profile and comparative analysis was carried out for MSE performance. To achieve this, modulated signal samples underwent a complex valued attenuation of $h_0 = \sqrt{0.1} \exp^{-j3\pi/4}$ and $h_1 = \sqrt{0.9} \exp^{j\pi/6}$, time delay of $\tau_0 = 0.5$ and $\tau_1 = -0.5$ and frequency offset of $\omega_0 = 2\pi \times 10^{-5}$ rad/sec. The channel gains are chosen to represent the case when bottom antenna transmits 90% of the total power while the top antenna transmits 10% of the total power. Again the time delays τ_0 and τ_1 were searched from the quantized subspace of size $2QN$ ($-QN$ to QN for $Q = 4$ and $N = 4$) using brute force method for function minimization as per (4.8c). In Fig. 5.8 the simulated mean squared errors for channel gain, time delay and frequency offset are plotted along with respective CRB. For all the modulation schemes (SOQPSK-TG, FQPSK-JR and SOQPSK-2T) the MSE plot for channel gain is overlapping on each other and together they are overlapping on the respecting CRB. Thus, for the case of channel gain the MSE performance [Fig. 5.8(a)] for SOQPSK-TG, FQPSK-JR and SOQPSK-2T are same and achieving the CRB. The same is true for MSE of frequency offset [Fig. 5.8(c)]. However, the time delay MSE [Fig. 5.8(b)] for all the three modulation schemes are overlapping on each other but not on the CRB. This is due to the fact that the time delay quantization parameter $Q = 4$ leads to smaller resolution in time. Overlapping with respective CRB can be achieved by increasing the time resolution (quantization parameter Q).



(a) Channel error variance



(b) Delay error variance



(c) Frequency offset error variance

Fig. 5.8. Comparison of MSE performance for SOQPSK-TG, FQPSK-JR and SOQPSK-2T by using sequential estimation method for level flight

Chapter 6

Conclusions and Future Work

In this thesis, periodically placed pilot sequences were utilized to estimate the frequency offset, timing delays and channel attenuation in STC encoded SOQPSK-TG based aeronautical telemetry system. A joint ML estimation of these three parameters was carried out. To overcome the computational complexity of joint estimation, a less complex sequential estimation was derived and analyzed. Subsequently, to reduce the computational complexity of the space time coded SOQPSK-TG decoder, pulse shaping was introduced in SOQPSK-TG frequency pulse. Frequency pulse of length 2 bit periods was used to generate SOQPSK-2T. SOQPSK-2T significantly reduces the STC decoder complexity due to lesser number of MLSE states. However, the 99% bandwidth of SOQPSK-2T is slightly more than that of SOQPSK-TG. Another Tier-II waveform for aeronautical telemetry, FQPSK-JR was space time coded for MSE performance evaluation by using sequential estimation method. The MSE performance for FQPSK-JR and SOQPSK-2T were found to be similar to that of SOQPSK-TG, and all three of them were found to be meeting the CRB.

Further to speed up the search over parameter space, faster search algorithms can be incorporated for estimator execution. Analytical assessment of STC decoder for space time coded SOQPSK-2T and FQPSK-JR based aeronautical telemetry systems could be carried out. Some other pulse shaping schemes could be explored to exactly match the SOQPSK-TG characteristics while limiting the pulse duration to 2 bit intervals.

Appendix A

Cramér–Rao Bound

In this appendix the CRB for ML estimation of frequency offset (ω_0), complex-valued Channel Gains (h_0 and h_1) and time Delays (τ_0 and τ_1) is provided (4.7). Conceptually CRB is defined only for real parameters. Thus (4.1) must be rearranged by separating the real and imaginary parts of \mathbf{h} . Because of this the ML estimate can be considered as the estimation of seven real-valued parameters (h_{R0} , h_{I0} , h_{R1} , h_{I1} , τ_0 , τ_1 and ω_0). This can be accomplished as follows

$$\begin{aligned}
 \mathbf{r} &= \mathbf{r}_R + j\mathbf{r}_I \\
 \boldsymbol{\Omega} &= \mathbf{C} + j\mathbf{S} \\
 \mathbf{P} &= \mathbf{P}_R + j\mathbf{P}_I \\
 \mathbf{h} &= \mathbf{h}_R + j\mathbf{h}_I \\
 \mathbf{w} &= \mathbf{w}_R + j\mathbf{w}_I
 \end{aligned} \tag{A.1}$$

By stacking the real parts over imaginary parts, (4.1) can be re-expressed as

$$\begin{bmatrix} \mathbf{r}_R \\ \mathbf{r}_I \end{bmatrix} = \begin{bmatrix} \mathbf{C} & -\mathbf{S} \\ \mathbf{S} & \mathbf{C} \end{bmatrix} \begin{bmatrix} \mathbf{P}_R & -\mathbf{P}_I \\ \mathbf{P}_I & \mathbf{P}_R \end{bmatrix} \begin{bmatrix} \mathbf{h}_R \\ \mathbf{h}_I \end{bmatrix} + \begin{bmatrix} \mathbf{w}_R \\ \mathbf{w}_I \end{bmatrix} \tag{A.2}$$

and in term of short-hand notation as

$$\mathbf{r} = \mathbf{Q}\mathbb{P}\mathbb{H} + \mathbf{w} \tag{A.3}$$

where \mathbf{r} and \mathbf{w} are vectors of size $2N_P \times 1$, \mathbb{H} is a 4×1 matrix, \mathbb{P} is a $2N_P \times 4$ matrix and \mathbf{Q} is a $2N_P \times 2N_P$ matrix. The log-likelihood function $\Lambda(\boldsymbol{\theta})$ for the unknown parameters is defined as

$$\Lambda(\boldsymbol{\theta}) = -\frac{1}{2\sigma^2} |\mathbf{r} - \mathbb{Q}\mathbf{P}\mathbf{H}|^2 \quad (\text{A.4})$$

where, $\boldsymbol{\theta}$ represents vector of parameters, defined as

$$\boldsymbol{\theta} = \begin{bmatrix} \mathbb{H} \\ \boldsymbol{\tau} \\ \omega_0 \end{bmatrix} \quad (\text{A.5})$$

Starting from the log-likelihood function mentioned above, the derivation of CRB was carried out in [5]. The Fisher information matrix is defined as

$$\mathbb{J} = \frac{1}{\sigma^2} \times \begin{bmatrix} \mathbb{P}^\top \mathbb{P} & \mathbb{P}^\top \mathbb{A}_0 \mathbb{H} & \mathbb{P}^\top \mathbb{A}_1 \mathbb{H} & \mathbb{P}^\top \mathbb{T} \mathbb{D} \mathbb{P} \mathbb{H} \\ \mathbb{H}^\top \mathbb{A}_0^\top \mathbb{P} & \mathbb{H}^\top \mathbb{A}_0^\top \mathbb{A}_0 \mathbb{H} & \mathbb{H}^\top \mathbb{A}_0^\top \mathbb{A}_1 \mathbb{H} & \mathbb{H}^\top \mathbb{A}_0^\top \mathbb{T} \mathbb{D} \mathbb{P} \mathbb{H} \\ \mathbb{H}^\top \mathbb{A}_1^\top \mathbb{P} & \mathbb{H}^\top \mathbb{A}_1^\top \mathbb{A}_0 \mathbb{H} & \mathbb{H}^\top \mathbb{A}_1^\top \mathbb{A}_1 \mathbb{H} & \mathbb{H}^\top \mathbb{A}_1^\top \mathbb{T} \mathbb{D} \mathbb{P} \mathbb{H} \\ \mathbb{H}^\top \mathbb{P}^\top \mathbb{D} \mathbb{T} \mathbb{P}^\top & \mathbb{H}^\top \mathbb{A}_0^\top \mathbb{T} \mathbb{D} \mathbb{P} \mathbb{H} & \mathbb{H}^\top \mathbb{A}_1^\top \mathbb{T} \mathbb{D} \mathbb{P} \mathbb{H} & \mathbb{H}^\top \mathbb{P}^\top \mathbb{D}^2 \mathbb{P} \mathbb{H} \end{bmatrix}$$

where, σ represents noise variance and, \mathbb{T} is a $2N_p \times 2N_p$ matrix defined as

$$\mathbb{T} = \begin{bmatrix} \mathbf{0}_{N_p} & -\mathbf{I}_{N_p} \\ \mathbf{I}_{N_p} & \mathbf{0}_{N_p} \end{bmatrix} \quad (\text{A.6})$$

where $\mathbf{0}_{N_p}$ and \mathbf{I}_{N_p} represents zero and identity matrix of size $N_p \times N_p$ and, \mathbb{D} is a $2N_p \times 2N_p$ matrix defined as

$$\mathbb{D} = \begin{bmatrix} \mathbb{D} & \mathbf{0}_{N_p} \\ \mathbf{0}_{N_p} & \mathbb{D} \end{bmatrix} \quad (\text{A.7})$$

where \mathbb{D} represents $N_p \times N_p$ diagonal matrix expressed as

$$\mathbb{D} = \begin{bmatrix} 0 & & & \\ & 1 & & \\ & & \ddots & \\ & & & (N_p - 1) \end{bmatrix} \quad (\text{A.8})$$

and, $2N_p \times 4$ matrices \mathbb{A}_0 and \mathbb{A}_1 are obtained by differentiating matrix \mathbb{P} with respect to delay τ_0 and τ_1 respectively. Matrices \mathbb{A}_0 and \mathbb{A}_1 are expressed as [5]

$$\mathbb{A}_0 = \left[\begin{array}{cc|cc} -Tp'_{0,R}(-\tau_0 T) & 0 & Tp'_{0,I}(-\tau_0 T) & 0 \\ -Tp'_{0,R}((1-\tau_0)T) & 0 & Tp'_{0,I}((1-\tau_0)T) & 0 \\ \vdots & \vdots & \vdots & \vdots \\ -Tp'_{0,R}((N_p-1-\tau_0)T) & 0 & Tp'_{0,I}((N_p-1-\tau_0)T) & 0 \\ \hline -Tp'_{0,I}(-\tau_0 T) & 0 & -Tp'_{0,R}(-\tau_0 T) & 0 \\ -Tp'_{0,I}((1-\tau_0)T) & 0 & -Tp'_{0,R}((1-\tau_0)T) & 0 \\ \vdots & \vdots & \vdots & \vdots \\ -Tp'_{0,I}((N_p-1-\tau_0)T) & 0 & -Tp'_{0,R}((N_p-1-\tau_0)T) & 0 \end{array} \right]$$

$$\mathbb{A}_1 = \left[\begin{array}{cc|cc} 0 & -Tp'_{1,R}(-\tau_1 T) & 0 & Tp'_{1,I}(-\tau_1 T) \\ 0 & -Tp'_{1,R}((1-\tau_1)T) & 0 & Tp'_{1,I}((1-\tau_1)T) \\ \vdots & \vdots & \vdots & \vdots \\ 0 & -Tp'_{1,R}((N_p-1)T - \tau_1) & 0 & Tp'_{1,I}((N_p-1)T - \tau_1) \\ \hline 0 & -Tp'_{1,I}(-\tau_1 T) & 0 & -Tp'_{1,R}(-\tau_1 T) \\ 0 & -Tp'_{1,I}((1-\tau_1)T) & 0 & -Tp'_{1,R}((1-\tau_1)T) \\ \vdots & \vdots & \vdots & \vdots \\ 0 & -Tp'_{1,I}((N_p-1-\tau_1)T) & 0 & -Tp'_{1,R}((N_p-1-\tau_1)T) \end{array} \right]$$

The co-variance matrix for obtaining estimation errors is formed by taking inverse of fisher information matrix (\mathbb{J}). The diagonal elements of matrix \mathbb{J}^{-1} represents CRB for the estimated parameters.

Bibliography

- [1] C. A. Balanis, *Antenna Theory Analysis and Design*, 3rd ed. Wiley Publication, 2005.
- [2] M. Jensen, M. Rice, and A. Anderson, “Aeronautical telemetry using multiple-antenna transmitters,” *IEEE Transactions on Aerospace and Electronic Systems*, vol. 43, no. 1, pp. 262–272, Jan 2007.
- [3] T. Nelson, E. Perrins, and M. Rice, “Near optimal common detection techniques for shaped offset QPSK and Feher’s QPSK,” *IEEE Transactions on Communications*, vol. 56, no. 5, pp. 724–735, May 2008.
- [4] M. Rice, T. Nelson, J. Palmer, C. Lavin, and K. Temple, “Space-time coding for aeronautical telemetry: Part II-decoder and system performance,” *IEEE Transactions on Aerospace and Electronic Systems*, vol. 53, no. 4, pp. 1732–1754, Feb 2017.
- [5] M. Rice, J. Palmer, C. Lavin, and T. Nelson, “Space-time coding for aeronautical telemetry: Part I-estimators,” *IEEE Transactions on Aerospace and Electronic Systems*, vol. 53, no. 4, pp. 1709–1731, Feb 2017.
- [6] IRIG 106-17: Telemetry Standards, Telemetry Group, Range Commanders Council, July 2017.
- [7] S. Horan, *Introduction to PCM Telemetry Systems*, 2nd ed. CRC Press, 2002.
- [8] S. Alamouti, “A simple transmit diversity technique for wireless communications,” *IEEE Journal on Selected Areas in Communications*, vol. 16, no. 8, pp. 1451–1458, Oct 1998.
- [9] E. Perrins and M. Rice, “Reduced-complexity approach to iterative detection of coded SOQPSK,” *IEEE Transaction on Communication*, vol. 55, no. 7, pp. 1354–1362, Jul 2007.

- [10] J. Proakis and M. Salehi, *Digital Communications*. New York: McGraw-Hill, 2008.
- [11] E. Perrins, “FEC systems for aeronautical telemetry,” *IEEE Transactions on Aerospace and Electronic Systems*, vol. 49, no. 4, pp. 2340–2352, Oct 2013.
- [12] E. Perrins and M. Rice, “Simple detectors for shaped-offset QPSK using the PAM decomposition,” in *IEEE Global Telecommunications Conference (GLOBECOM)*, Nov 2005, pp. 408–412.
- [13] M. Simon, “Multiple bit differential detection of offset quadrature phase-shift-keying,” in *IEEE International Conference on Communications (ICC), Anchorage, AK, USA*, vol. 4, May 2003, pp. 2817–2821.
- [14] Lifang Li and M. K. Simon, “Performance of coded OQPSK and MIL-STD SOQPSK with iterative decoding,” *IEEE Transactions on Communications*, vol. 52, no. 11, pp. 1890–1900, Nov 2004.
- [15] T. J. Hill, “An enhanced, constant envelope, interoperable shaped offset QPSK (SO-QPSK) waveform for improved spectral efficiency,” in *International Telemetry Conference, San Diego, CA, USA*, Oct 2000, pp. 127–136.
- [16] M. K. Simon and T. Y. Yan, “Performance evaluation and interpretation of unfiltered Feher-patented quadrature phase-shift keying (FQPSK)”, Telecommunications and Mission Operations Progress Report, Jet Propulsion Laboratory Std., May 1999.
- [17] P. Leung and K. Feher, “F-QPSK: A superior modulation technique for mobile and personal communications,” *IEEE Transactions on Broadcasting*, vol. 39, no. 2, pp. 288–294, June 1993.
- [18] R. P. Jefferis, “Evaluation of constant envelope offset quadrature phase shift keying transmitters with a software based signal analyzer,” in *International Telemetry Conference, San Diego, CA, USA*, Oct 2004.
- [19] T. Nelson, E. Perrins, and M. Rice, “Common detectors for shaped offset QPSK (SO-QPSK) and Feher-patented QPSK (FQPSK),” in *IEEE Global Telecommunications Conference (GLOBECOM)*, vol. 6, Nov 2005, pp. 3743–3747.
- [20] M. Geoghegan, “Description and performance results for a multi-h CPM telemetry waveform,” in *21st Century Military Communications (MILCOM). Architect-*

tures and Technologies for Information Superiority (Cat. No.00CH37155), vol. 1, Oct 2000, pp. 353–357.

- [21] M. Rice, “Space-time coding for aeronautical telemetry: Part I-System description,” in *International Telemetry Conference, Las Vegas, NV, USA*, 2011.
- [22] —, “The challenges of C-band missile telemetry,” in *International Telemetry Conference, San Diego, CA, USA*, Oct 2012.
- [23] Y. S. Cho, J. Kim, W. Y. Yang, and C. G. Kang, *Wireless Communications with MATLAB, MIMO-OFDM*. Wiley Publishing, 2010.
- [24] J. B. Anderson, T. Aulin, and C. E. Sundberg, *Digital Phase Modulation*. New York, NY, USA: Plenum Press, 1986.
- [25] T. Aulin and C. E. Sundberg, “Continuous phase modulation - Part I: Full response signaling,” *IEEE Transactions on Communications*, vol. 29, no. 3, pp. 196–209, Mar 1981.
- [26] T. Aulin, N. Rydbeck, and C. E. Sundberg, “Continuous phase modulation - Part II: Partial response signaling,” *IEEE Transactions on Communications*, vol. 29, no. 3, pp. 210–225, Mar 1981.
- [27] M. Rice and A. McMurdie, “On frame synchronization in aeronautical telemetry,” *IEEE Transactions on Aerospace and Electronic Systems*, vol. 52, no. 5, pp. 2263–2280, Oct 2016.
- [28] M. Chiani, “Noncoherent frame synchronization,” *IEEE Transaction on Communication*, vol. 58, no. 5, pp. 1536–1545, May 2010.
- [29] D. I. S. Agency, “Department of defense interface standard, interoperability standard for single-access 5-kHz and 25-kHz UHF satellite communications channels,” MIL-STD-188-181B, Department of Defense, Tech. Rep., Mar 1999.